Focused Ultrasound for the Generation of Cancer Immunotherapy

By

Mary Diana Dockery

Thesis

Submitted to the Faculty of the

Graduate School of Vanderbilt University

in partial fulfillment of the requirements

for the degree of

MASTER OF SCIENCE

in

Biomedical Engineering

December, 2016

Nashville, Tennessee

Approved:

Todd D. Giorgio, Ph.D.

Charles F. Caskey, Ph.D.

To my mom and dad, for your life-long encouragement in all of my pursuits

and

To my beloved fiancé, Marty, for your boundless support

ACKNOWLEDGEMENTS

This work was supported by the Office of the Assistant Secretary of Defense for Health Affairs through the Breast Cancer Research Program under Award No. (W81XWH-13-1-0231). Opinions, interpretations, conclusions, and recommendations are those of the author and are not necessarily endorsed by the Department of Defense. This work would not have been possible without the support of the shared resources available through Vanderbilt University and Vanderbilt University Medical Center (VUMC). I acknowledge the Translational Pathology Shared Resource supported by NCI/NIH Cancer Center Support Grant 2P30 CA068485-14 and the Vanderbilt Mouse Metabolic Phenotyping Center Grant 5U24DK059637-13. Whole slide imaging was performed in the Digital Histology Shared Resource at Vanderbilt University Medical Center (www.mc.vanderbilt.edu/dhsr). Flow Cytometry experiments were performed in the VUMC Flow Cytometry Shared Resource, which is supported by the Vanderbilt Ingram Cancer Center (P30 CA68485) and the Vanderbilt Digestive Disease Research Center (DK058404). I am especially grateful to David K. Flaherty for his endless guidance, answers, and patience during the development and implementation of all flow cytometry experiments.

I wish to thank two of my mentors, Dr. Matthew Walker III and Dr. Fiona Yull, who have helped me improve my research and find myself beyond the science. I am thankful to my collaborators, lab members, and everyone who has aided in the completion of this work. Particularly, Dr. Charles Caskey has had an integral role providing scientific direction. I would especially like to thank my mentor and research advisor, Dr. Todd Giorgio, for the personal and professional guidance he has given.

My family and friends have been infinitely supportive of me throughout this project. I want to thank my parents for their unconditional love. They are incredible role models for the hard work and endurance needed for success. Finally, I would like to thank Marty, my loving fiancé and best friend. His constancy, support, and culinary skills have been invaluable.

TABLE OF CONTENTS

LIST OF TABLES

LIST OF FIGURES

CHAPTER I

ULTRASOUND-INDUCED CANCER IMMUNOTHERAPY: PRIMED FOR SUCCESS?

Background Overview

Significant advances in breast cancer research have led to improvements in screening and therapy, including breast conserving surgery[1], platinum-based chemotherapies[1,2], tumor cell receptor-targeted therapies[1–3], angiogenesis-targeted therapies[2], cell cycle-targeted therapies[2,3], and immune therapies[2]. Breast cancer, however, is still the second leading cause of cancer related deaths in women. General medicine, and cancer in particular, have experienced a fundamental shift in the focus of research; the idea of 'one size fits all' medicine is being revised by the understanding that patient-to-patient differences render effects of identical treatments from potent in some patients to ineffective in others. The result has been a paradigm transformation with the goal of generating robust therapeutic response in all patients based on therapeutic approaches tailored and personalized for each individual.

One promising branch of personalized cancer research is immunotherapy, in which treatments aim to enhance and arm a patient's own immune system against tumor cells. The immune system is an ideal therapeutic option for cancer given its basic attributes for targeting specificity, systemic surveillance, and long-term memory. While normally effective for anti-tumor surveillance, cancer immunity can be reduced by accumulated changes in the tumor microenvironment[4].

The potential for immunotherapy is evidenced by reports dating back centuries[5,6], long before the elucidation of specific immune involvement and mechanisms. More recently, a number of cancer immunotherapies have been developed from the personalized era of medicine, including monocloncal antibodies[7–9], adoptive T cell transfer[4,10,11], and the infusion of donor immune cells[12]. Despite promise,

these treatments have demonstrated drawbacks and limitations discussed below in the "Cancer and the Immune System" section.

Another less-explored cancer immunotherapeutic option involves generating acute local inflammation intended to overcome tumor microenvironment-induced immune suppression[4,13]. Furthermore, numerous cases have been reported of an 'abscopal' effect – or distant bystander effect – where local inflammatory treatments in tumors, even of a palliative nature, trigger regression of distant, untreated tumors[14–16]. Research focused on eliciting this immune-mediated abscopal effect holds significant promise for metastatic disease, but variation among methods and resulting reports of efficacy is a barrier to progress[14]. One specific method for inducing systemic immunity to cancer, which holds considerable promise, involves the use of therapeutic ultrasound[17]. In this overview, we address the fundamental principles of cancer, immunology, and therapeutic ultrasound, and examine evidence supporting ultrasound-induced cancer immunotherapy.

Breast Cancer Basics

One in eight women will be diagnosed with breast cancer in her lifetime.[18] Breast cancer is primarily classified into three categories based on gene expression profiling and receptors available for targeted therapy.[19] Luminal cell breast cancers typically overexpress estrogen receptors (ER+), progesterone receptors (PR+), or both (ER+/PR+).[19] Human endothelial growth factor receptor (HER2+) breast cancers overexpress HER2, a membrane receptor of the epidermal growth factor receptor family.[3,19] While ER/PR/HER2 status provide options for targeted therapeutics, basal cell breast cancers generally lack targetable receptors (ER-/PR-/HER2-) and are referred to as triple negative breast cancers.[19] The identification of unique molecular markers for HER2+ and ER+/PR+ breast cancers have led to the development of targeted therapeutics, but *de novo* resistance and acquired resistance continue to limit success of targeted therapies[1,8]. Breast tumors are often heterogeneous in their cellular composition,

further complicating therapeutic efforts. While targeted therapies are often effective for the majority of cell types in a tumor, remaining cells may continue disease progression along with any targeted cells that have acquired resistance to therapy.[1,8]

The primary concern associated with breast cancer is metastatic progression resulting in functional impediment of vital organs[18]. In the United States, improved screening has led to an increase in early stage breast cancer diagnoses, but no significant change in the number of cases which are metastatic disease at initial presentation (Figure 1)[20]. Even with the use of treatment options for primary breast cancer, including surgical tumor resection, removal of downstream lymph nodes, radiation therapy, chemotherapy, and targeted therapies, 20-30% of invasive breast cancer patients will develop recurrent disease, often at metastatic sites.[18,21] Whether metastatic at initial diagnosis or with disease recurrence, no cure exists for metastatic breast cancer, lending to a median survival of 3 years once metastatic disease is identified.[18,22] Development of effective, durable therapies for metastatic disease is a challenge that must be overcome to eliminate the mortality associated with breast cancer.

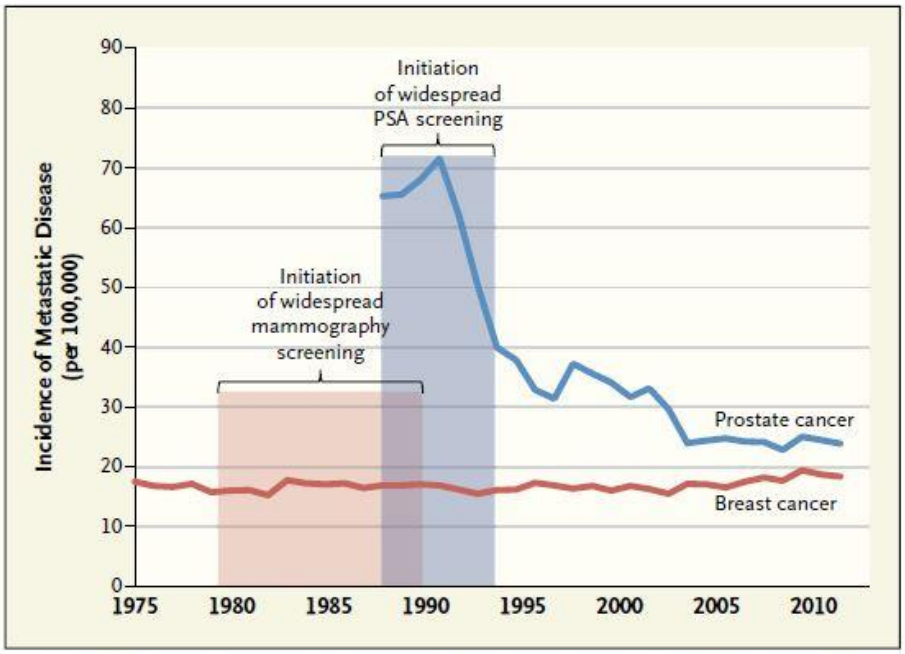

Figure 1. Incidence of cancer that was metastatic at first presentation, United States, 1975-2012. Data are for breast cancer (SEER historic stage distant) among women 40 years of age or older and prostate cancer (American Joint Committee Stage IV) among men 40 years of age or older. Reproduced with permission from Welch et al,[20] Copyright Massachusetts Medical Society.

Immunology Basics

The immune system, designed to protect the host from foreign invaders, is a complex, multi-layered network. The first layer provides a physical barrier to help prevent initial invasion of the host[13,23]. This layer comprises the skin and mucous membranes.[23,24] Any discontinuity in the barrier, however, such as a wound, provides a direct path for microorganisms to enter and attack the host. Innate immunity, the second layer of immune defense, provides a rapid immune response to trap and eliminate foreign bodies[23–25]. Adaptive immunity is the third layer of the system, and has been identified in approximately 1% of animals[23]. The adaptive response is tailor-made ("adapted") to target a specific invader, and to create a thorough, effective elimination of the foreign microorganism[25].

The innate and adaptive systems have distinctly separate, broad functions in an immune response. The innate system is the rapid-response team. It simultaneously isolates the affected tissue, launches a primary defensive attack on the assailing microorganism, and recruits other immune cells to the site for assistance.[23–25] Cells of the body express "self" surface markers which indicate to immune cells that they are not a threat and do not warrant an attack by the immune system.[23,25] Invading pathogens do not express the same markers as the host's "self" cells, but instead express other unique surface markers, as well as some which are common among microorganisms.[23–25] These surface markers allow cells of the innate system to identify "non-self" cells as foreign invaders. While sufficient to eliminate small infections, the innate system is incapable of mounting a robust attack without aid.[23]

Adaptive immunity, as its name suggests, is designed to adapt to a specific, existing threat.[23–25] To activate this arm of the immune response, the innate system alerts the adaptive system to the foreign presence and provides information about the invader.[23–25] The adaptive system tailors some of its cells based on information from the invaders to develop cells specifically able to grow, divide, and eliminate the threat.[23,25] This response is robust in both cell number and targeting specificity; however the need to modify and then expand cells to generate a significant response requires time, up to a week for some adaptive cell types.[23,25] The adaptive system provides an additional benefit – once the infection has been eliminated, most of the adaptive cells involved in the specific response are eliminated because there is no longer a need for them, but a few are kept in circulation.[23,25] These circulating cells impart a memory capacity to the host's immunity and are capable of mounting a substantially faster response if that invader is subsequently encountered in the future.[23,25] An effective way to leverage this aspect of immunity is vaccinations, which present the body with a dead or weakened form of a microorganism to induce adaptive memory cells; if the active pathogen is encountered later, the body responds in a rapid and robust manner to eliminate the infection[23].

Cancer and the Immune System

In addition to targeting "non-self" invading pathogens, the immune system is also able to differentiate "self" cells from "altered-self" cells[11,26]. For example, tumor cells express altered levels and mutated versions of normal "self" surface markers making them identifiable by immune cells[26]. Despite the broad capacity of the immune system, tumors are highly adaptable, enabling changes that reduce immunorecognition.[27] Accumulated mutations eventually modify the tumor microenvironment, including cells in the tumor and surrounding tissue, toward pro-tumor, anti-host activity.[27–30] Immunoediting is the process by which the tumor cells interact with the host's immune system, and it encompasses the induced immune-suppressor/tumor-suppressor dichotomy.[28–30] The immunosuppressive nature of tumors stems from a variety of mechanisms working together to limit recruitment of activated immune cells, down-regulate stimulatory ligands, up-regulate immune inhibitory signaling, and elevate retention of immune regulatory cells.[11,31] Tumors are typically in a protective state of mild, chronic inflammation resembling a healing wound[4,32,33]. As such, generating an acute inflammatory response in the tumor may recruit immune cells into the microenvironment, subverting the immune suppressive tumor mechanisms[34]. The characteristics of the immune system make it perfectly poised for an effective anti-tumor response, specifically three primary attributes: 1) ability to distinguish self from altered-self, 2) high specificity of the adaptive immune response, and 3) the long-term retention of immune memory cells for systemic surveillance

In 1891, William B. Coley demonstrated some of the first evidence for immune modulation in tumors as a potential treatment option.[5] Limitations in understanding the immune system caused many in the field to doubt Coley's findings. The advent of radiation and chemotherapy as effective cancer treatments ended the search for immunotherapy options.[5,7] Cancer-related immune research did not resurface until 1957 when Frank McFarlane Burnet proposed that the immune system could distinguish between cancer cells and normal cells.[7,35] Subsequent immunotherapy research, particularly in recent

decades, has demonstrated high potential and moderate success at both local and systemic levels. Currently approved immune-based cancer therapeutics have been summarized by Li, et al in Table 1.[7]

Table 1. Examples of FDA-approved cancer immunotherapeutic agents. (Table reproduced from Li et al.,[7] with permission license provided by Creative Commons.[36])

Modality	Principle
Hematopoietic stem cell transplantion (e.g., leukemia and myeloma)	1. Reset the immune system
	2. Allo-antigen response (graft versus tumor effect)
Antibody (e.g., retuximab, trastuzumab)	1. Eliminate cancer cells
	2. Block key signaling pathways
Cytokines (e.g., type I interferon, interleukin-2)	Boost both innate and adaptive immunity
Dendritic cells (e.g., Sip-T for prostate cancer)	Enhance tumor-specific T cell priming
T cell checkpoint blockade (e.g., Ipilumimab for melanoma)	Block/reverse immune tolerance
Microbes (e.g., BCG for the transitional bladder cancer)	Enhance innate and adaptive immunity

Antibody therapies rely on mutated surface expression ("altered self") of cancer cells, and act through surface receptors, immune modulation, or conjugated drug delivery[8]. Significant limitations lie in short circulation half-life[9], off target effects from systemic administration[9], and resistance, both *de novo* and acquired[37]. Tumor vaccination and T cell transfer methods both aim to arm the patient's adaptive immune cells by providing the cells with the 'best' tumor-targeting antigens on an individualized patient level[4]. These options are limited by immune competence of the patient, suppressive tumor microenvironment, and resistance[4].

Evidence of anti-tumor immune stimulation at sites distant to the local site of treatment, the abscopal effect, provides precedent for localized immunotherapy as an effective treatment for metastatic disease[14,15]. Optimal immunotherapy would engage adaptive immunity to generate a therapeutic response which specifically targets a patient's unique tumor cells, systemically clears metastatic tumors, and effectively retains memory cells to eliminate recurrent tumors. Ultrasound is one promising method to induce the localized acute inflammation needed for such immunotherapeutic options[38].

Ultrasound

Diagnostic ultrasound is a non-invasive, non-ionizing imaging technique, making it safe for many applications, including pre-natal imaging. Ultrasonic technology also has applications in a therapeutic capacity, which were recognized in 1927, even before its potential for diagnostics[38,39]. Research into therapeutic ultrasound has increased in recent years due to the availability of improved technology to generate and accurately measure ultrasound power[40]. Diagnostic ultrasound operates at a frequency of approximately 5 MHz, while the therapeutic range is 20 kHz to 3 MHz[41] (see Figure 2). Ultrasonic therapies fall into two general categories of power: low and high[38]. Low power uses include transdermal delivery of topical drugs and vaccines[17,42], sonoporation[38], thrombolysis[17,43], and physiotherapy[17,40]. High power ultrasound is employed in treatment of kidney stones[40] and tumors[17,38,40].

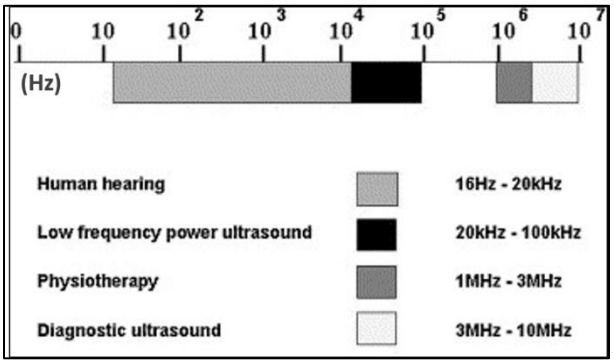

Figure 2. General classification of the frequency ranges of ultrasound. (Figure adapted and reprinted from Ultrasonics Sonochemistry, 11(2), Yu *et al,* A review of research into the uses of low level ultrasound in cancer therapy, Pages 95-103, Copyright 2004, with permission from Elsevier .[40])

Different than diagnostic ultrasound, which seeks to limit cellular effects,[38,41] therapeutic ultrasound aims to create effects, reversible and permanent, at the cellular level.[38] Biological effects of therapeutic ultrasound can be precisely tuned with selection of ultrasound parameters for controlled energy deposition in tissue, specifically the amount and type of energy, which may be thermal, mechanical, or a combination.[38,44,45]

Generation of a thermal increase in a targeted tissue has numerous biological consequences, ranging from mild hyperthermia to thermal ablation. Thermal change is created when the tissue incident to the beam absorbs energy from the ultrasonic waves[46]. The effects of thermal therapy are dependent on a number of characteristics including physical tissue properties (i.e. size, density, perfusion), thermal properties of tissue, peak temperature applied, and duration of thermal application.[46,47] To account for these variations, the cumulative equivalent minutes at 43 ^{o}C (CEM43) calculation was developed for quantitative dosimetry during thermal therapeutics.[48] Analysis of compiled temperature-death data from cells in vitro by Dewey,[49] found that above 43 ^{o}C thermal treatment of cells in vitro resulted in exponential cell death.[47] The equation is CEM43 = $\int_0^i t_i * R^{(43-T_i)}$, where t is the given time interval (i), T is the average temperature during the interval 0:i, and R is a term to account for temperature-related cell death, where R = ¼ for T_i less than 43 ^{o}C, and R = ½ otherwise.[47] This provides a useful quantitative measure of thermal dosing, which can be compared across methods and instruments to overcome dosimetry differences and limit the subsequent variability of reported bioeffects. Recent advances in magnetic resonance (MR) technology have led to the development of MR-thermometry, a technique for thermal mapping which utilizes temperature-based changes in proton-resonance.[50,51] MR-thermometry may be used in conjunction with therapeutic ultrasound to precisely measure thermal changes in tissue, which can be mapped onto an MR image, in real time, to display CEM43 as a function of time.[50,52,53]

Mechanical ultrasound events are generated with large pressure oscillations over short pulses of application.[54] Acoustic streaming and acoustic cavitation are two types of mechanically-induced biological effects of ultrasound. Acoustic streaming relates to the motion experienced by molecules and organelles in the path of ultrasound propagation. Structures held in place by adhesions and extracellular matrix remain fixed, while fluid and small molecules are free to flow around the stationary objects. Acoustic cavitation relies on the presence of stable gas microbubbles in the tissue, which interact with the pressure oscillations causing miniature explosions, subsequently damaging surrounding tissue.[55] Similar to the

quantification of ultrasound thermal dosimetry by CEM43, the mechanical effect of therapeutic ultrasound is measured with mechanical index (MI).[56] The MI is related to peak negative pressure of the pulse divided by the center frequency.[44,56,57] Shortcomings have been identified with MI, including the absence of a term to account for exposure time[44], temperature of the tissue[44], and multiple exposures[56].

FUS-Induced Anti-Tumor Immune Response

Previous studies have examined FUS in the context of tumor treatment[54]. Many early studies primarily used FUS for non-invasive ablation of tumors as a surgical alternative.[50,53,58,59] A variety of FUS treatment parameters have been examined to assess the immunostimulatory impacts in the tumor milieu. Hu et. al. compared mechanical and thermal FUS *ex vivo* and determined that debris from tumors treated with mechanical FUS more effectively stimulated dendritic cells and macrophages for anti-tumor activity.[60,61] Some additional studies of FUS-induced anti-tumor immune response include: sparse arrangement of small, thermal lesions within tumors to avoid whole-tumor ablation,[62] sub-ablative levels of hyperthermia for moderation of the tumor microenvironment and immune activity,[63] sub-ablative hyperthermia in combination with immunomodulatory agents,[64] and the use of FUS for tumor vaccine strategies.[65,66]

Conclusion

The promise held by cancer immunotherapy has transitioned research towards more immuno-centric goals. Previous studies in cancer, immunotherapy, and FUS result in an expansive field with exciting potential for the synthesis of effective FUS-induced anti-tumor immunotherapies. Specifically, there is a need for an experimental framework which thoroughly, reproducibly, and quantitatively assesses response to treatment. The complexity of immune cells involved, their respective response

kinetics, and microenvironmental signaling processes necessitates the use of multiplexed response characterization to conclusively infer therapeutic efficacy.

Cancer immunotherapy has the potential to revolutionize the standards to cancer therapy and prognosis. While generating relevant, durable immunotherapeutic responses has proved difficult, substantial evidence suggests its clinical feasibility. Therapeutic ultrasound is a promising method for cancer immunotherapy given its non-invasive, non-ionizing nature, and highly tunable properties.

CHAPTER II

FOCUSED ULTRASOUND INDUCED CANCER IMMUNOTHERAPY IN A MAMMARY TUMOR MODEL

Background Overview

The application of focused ultrasound to tumors in a murine model of breast cancer was used for the purpose of generating an anti-tumor immune response. A critical component required for thorough characterization of response to FUS-induced cancer immunotherapy involves evaluation of the cellular responses as a function of stimulus. In this study, we use a reporter mouse model of spontaneous breast cancer for *in vivo* bioluminescent imaging to track NF-κB activation, which is a central mediator of inflammation and cancer development processes.[67–70] The time course of NF-κB activation is used to inform the timing of tissue isolation for immune assessments. Treated, untreated, and contralateral tumor tissues and spleens were analyzed by flow cytometry, immunohistochemistry (IHC), and cytokine bead array to characterize changes in the cellular and effector response following FUS.

Cancer Immunotherapy Targets and Barriers

Cancer immunotherapy takes the concept of personalized medicine to arm a patient's own immune system against their unique tumor cells. Successful induction of anti-tumor immunity has been demonstrated to produce complete, lasting remission in patients, but responses have been inconsistent[11,71–73]. Complexities of the immune system, such as response to environmental signaling and activation/suppression balance, complicate reproducible success of anti-tumor immunotherapies.

Immune cells in the tumor microenvironment are subject to tumor-produced cytokines and other signaling effectors, which shift immune cells to pro-tumor phenotypes, suppressing anti-tumor

responses[31,74–76]. Many therapies seek to activate immune cells and inhibit immune suppressors with the goal of shifting the anti-tumor/pro-tumor dichotomy towards an anti-tumor effect. Dendritic cell vaccines[77] and adoptive T cell transfer[10,11,78] seek to activate immune cells in a manner specifically targeted to tumor cells, while antibodies against cytotoxic T lymphocyte associated antigen 4 (CTLA-4)[79,80], programmed cell death protein 1 (PD1)[79–82], and programmed cell death ligand 1 (PD-L1)[81] target immune checkpoints to selectively suppress immunoregulation. Immunotherapy research has spanned the range of the immune system: dendritic cells[62,83–86], macrophages[33,87], and T lymphocytes[10,88] are a few of the immune targets currently being explored.

As adaptive immune cells, T lymphocytes are of particular interest due to their capacity to target tumor cells with high specificity in virtually all tissues[7,11,89], and retain a population of memory T cells for long-term surveillance[7,11]. Multiple T cell phenotypes exist and serve immunostimulatory and immunosuppressive roles in the tumor microenvironment[34,90]. Cytotoxic T lymphocytes (CTLs) have been identified as a key player in effective tumor elimination, directly engaging with, and destroying, tumor cells[88,91]. Helper T cells (T_{helper}) have an immune-supportive role, assisting and maintaining CTL activation through a variety of mechanisms, including interactions with antigen-presenting cells and production of stimulatory cytokines[92,93]. Additionally, T_{helper} cells help CTLs develop a subset of memory cells, necessary for potential long-term, anti-tumor response to recurrent disease[92,93]. In contrast to these two immunostimulatory T cell phenotypes, regulatory T cells (T_{regs}) serve an immunosuppressive role. In non-tumor environments, T_{regs} are critical in proper maintaining proper immune functionality, serving as a negative feedback control in the balanced system[93–96]. T_{regs} balance CTL activation to ensure that the magnitude of immune response is appropriate to the present threat, and to end the response once the threat is eliminated[95]. In the tumor milieu, however, T_{reg} activity has a tumor-supportive/immunosuppressive function, preventing activation of CTLs and forestalling cytotoxic elimination of tumor cells[92,96]. Cell phenotypes are identified with antibody labeling for phenotype-specific

cellular markers. T cells are generally discerned by the presence of CD3 surface receptor[97], and subsequent phenotypes can be distinguished by presence of CD8 (CTLs)[98,99], CD4 ($T_{helpers}$ and T_{regs})[95], and FoxP3 (T_{regs})[95]. The amount and phenotype of T cell infiltrates within tumors have prognostic value for response to immunotherapy[100]. Additionally, studies have identified increased CD4+/CD8+ T cell ratio as evidence of an anti-tumor response, further indicating the critical supportive role of CD4+ $T_{helpers}$[90]. The Immunoscore technique, developed to describe the distribution of immune phenotypes in the tumor, is an effective prognostic measure for immunotherapeutic response[101,102].

Barriers, both physical and chemical, are created by tumors to evade immune detection and limit immunogenicity[4]. Generation of effective anti-tumor immunity requires two key components: 1) infiltration of immune cells into the tumor, and 2) reversal of the tumor microenvironment (TME) for anti-tumor activation of the tumor-infiltrating immune cells. Acute inflammation (i.e. injury and infection) induces immune cell recruitment, providing a direct method to overcome some tumor barriers. Induction of an injury in the tumor may cause sufficient inflammation to recruit immune cells under the pretense of wound-healing. Once inside the tumor, immune cells may be able to recognize, target, and eliminate tumor cells. Immune cells, particularly those of the adaptive system, depend on protein-based antigen expression by tumors to develop tumor cell-specific recognition targeting. We hypothesize that the induced injury must be sufficient to elicit acute inflammation without denaturing the tumor-specific antigens which drive adaptive immune recognition patterning.

Cytokines in the Tumor Microenvironment

Cytokines are signaling molecules that serve as indirect lines of communication between cells, with a prominent role in the processes of immune cells[23,103]. The ability of cytokines to activate or suppress immune response is of particular interest for cancer immunotherapy research[103,104]. Interleukin (IL)-2 and interferon (IFN)-α are two cytokines approved by the FDA for the treatment of melanoma, with IFN-α also

approved to treat metastatic renal cell carcinoma[103]. The prevalence of signaling network redundancies and pleiotropic functions are limitations for cytokine-based immunotherapies and necessitate multiplexed cytokine measurements to characterize tumor immune environment[103,104]. This brief overview serves to identify and broadly classify the effects of several key cytokines in the tumor immunotherapy milieu.

Table 2 (adapted from Lee et al[103]) summarizes seven cytokines and several of their primary roles in immune signaling. IL-1β is involved in dendritic cell maturation, critical for effective antigen presentation to naïve T cells[103]. A pro-inflammatory subclass of T_{helper} cells, type 1 T_{helper} cells (Th1), are the primary source of IL-2, a cytokine necessary to achieve a robust anti-tumor immune response with sufficient activation and expansion of T cells.[103]. Tumor necrosis factor (TNF) is a potent immunostimulatory cytokine that can induce killing of tumor cells via recruitment and activation of macrophages, neutrophils, natural killer cells, and DCs[23,103]. Another strong immunostimulatory cytokine, interferon gamma (IFN-γ), is produced by a variety of immune cells, including T_{helper} cells, macrophages, and NK cells, to activate macrophages, increase expression of MHC class I and class II molecules for improved antigen presentation, and encourage T_{helper} differentiation of CD4+ T cells[103]. IL-6 acts as a potent immunostimulatory cytokine, promoting T cell proliferation, CD8+ T cell infiltration into tumors, and shifting naïve CD4+ T cells towards a T_{helper} 17 (Th17) phenotype instead of a suppressive Treg phenotype[105]. Th17 cells produce IL-17, IL-2, TNF, and IFN-γ, and generate a pro-inflammatory response which may be important in anti-tumor immunity[106]. In contrast to the anti-tumorigenic effects of these pro-inflammatory cytokines, effects of IL-10 are predominantly immunosuppressive including increased generation of T_{regs}, as well as down-regulation of MHC class II expression on—and inhibition of—macrophages and DCs[103].

While some primary functions of individual cytokines have been described here, this summary presents a simplified view of inherently complex signaling interactions. Recent research in the field

indicates that cytokines are produced by—and act upon—a variety of cell types[103]. As a result, each cytokine influences a multitude of immunological effects, both immunostimulatory and immunosuppressive, dependent upon the specific context of interest[103,105].

Table 2. General features of select cytokines. (Table adapted from Lee and Margolin[103], with permission license provided by Creative Commons[107]. *Sompayrac[23])

Cytokine	Primary Cell Source	Primary Target Cell	Biological Activity	Tumor Immunity Role
IL-1β	Monocytes Macrophages Fibroblasts Epithelial cells Endothelial cells Astrocytes	T cells B cells Endothelial cells Hypothalamus Liver	Co-stimulation Cell activation Inflammation Fever Acute phase reactant	Anti-Tumor
IL-2	T cells NK cells	T cells NK cells B cells Monocytes	Cell growth/ activation	Anti-Tumor
IL-6	T cells Macrophages Fibroblasts	T cells B cells Liver	Co-stimulation Cell growth/activation Acute phase reactant	Anti-Tumor
IL-10	Th2 T cells	Macrophages T cells	Inhibits antigen-presenting cells Inhibits cytokine production	Pro-Tumor
IL-17*	Th17	B cells	Recruit neutrophils Activate complement system	Anti-Tumor
TNF-α	Macrophages T cells	T cells B cells Endothelial cells Hypothalamus Liver	Co-stimulation Cell activation Inflammation Fever Acute phase reactant	Anti-Tumor
IFN-γ	T cells NK cells NKT cells	Monocytes Macrophages Endothelial cells Tissue cells	Cell growth/activation Enhances MHC expression	Anti-Tumor

Therapeutic Development Limitations

Advances in cellular and molecular analysis techniques have improved mechanistic understandings of disease and response to therapy. However, the need for biological samples (i.e. tissues) is a limiting factor in research progress. There is a need for methods to inform time point decisions for tissue collection. The temporal, dynamic changes in immune response to stimulus often require the collection of tissue samples at multiple time points to assess immune kinetics. This can be challenging due to the destructive nature of tissue recovery, which often necessitates collection of whole organs for animal models and biopsy specimens for human studies. While theoretically optimal, cellular and molecular analysis of biological samples collected at multiple time points has practical limitations, including time and financial feasibility. A statistically significant number of animals are needed at each time point, for each treatment group and corresponding control groups. Furthermore, sufficiently high sampling frequency in the temporal dimension is required to develop a representative view of the response, like an immune Nyquist frequency. Researchers must, therefore, select a limited number of collection time points to maintain experimental feasibility; however, if the time points selected are misguided, the tissue-based characterizations may not accurately represent the biological dynamics due to under sampling.

Bioluminescence in vivo *Imaging*

Development of *in vivo* imaging techniques, such as MR imaging, positron emission tomography, and bioluminescent imaging (BLI), have created an opportunity to monitor specific aspects of therapeutic response in animal studies with minimal invasiveness[108]. Imaging may be used to acquire data multiple times within a subject, including pre- and post-treatment information, so that controls may be subject-relative. Compared to other *in vivo* imaging methods, BLI technology affords imaging which is relatively simple, low cost, high sensitivity, and non-ionizing[109–111]. Typically, the firefly luciferase gene is transfected

into a DNA sequence downstream of a selected promoter sequence, such that promoter activation results in luciferase protein production[110,112]. Luciferin is then introduced (injected *in vivo* or with media *in vitro*) and, in the presence of oxygen and ATP, is oxidized by luciferase to form oxy-luciferin, which emits a photon in the process of relaxing from an excited state to ground state[110,112,113]. These photons scatter through the tissue and are detected by a charge-coupled device (CCD) camera, which bins photons, according to user-defined settings, to spatially identify bioluminescent sources[109]. The resulting two-dimensional photon map is overlaid on a photograph, acquired in tandem with BLI, for bioluminescent information which is co-registered with subject anatomy[109]. A variety of transgenic models have been developed for BLI, including transplantable cell lines, constitutively active spontaneous tumor models, and conditional activation models[108,112,114,115]. In this way, biological events coupled to the production of luciferase can be non-destructively and quantitatively characterized in complex living subjects by BLI.

Integral Role of the NF-κB Pathway in Cancer

Ubiquitous as a transcription factor, NF-κB is critically involved in many biological functions and is the basis for an expansive field of published literature.[116–118] This brief overview of NF-κB serves only as a primer for some of the functions which are most relevant in the context of the experimental work described here, and is not an exhaustive review of its effects. NF-κB plays a variety of roles in cancer and immunity dependent upon cell type and stage of tumor development, and is a central mediator of processes involved in tumor growth, apoptosis inhibition, metastatic progression, and inflammation, both chronic and acute[67,69,70,119–123]. Within the context of immunity, NF-κB is involved in processes of immune cell development,[69,124] production of immunomodulatory cytokines,[67,113,122,125] and leukocyte recruitment by regulation of adhesion molecules.[122] Furthermore, studies have demonstrated a duality: NF-κB activity may be pro-tumor or anti-tumor depending on cellular and environmental context.

Experimental Overview

We have generated a novel double-transgenic murine reporter model of cancer. This new model, PyNGL, incorporates spontaneous tumor formation and metastatic disease progression characteristics of the MMTV-PyMT (Polyoma) model of breast cancer[126] with *in vivo* NF-κB pathway reporter capabilities of the NF-κB-GFP-luciferase (NGL) model[112]. The immunocompetence of both the MMTV-PyMT and NGL models is supportive of PyNGL immunocompetence, with spontaneous formation of multiple mammary fat pad tumors, potential for metastatic progression to lungs, and the NF-κB reporter for *in vivo* bioluminescent imaging. PyNGL tumors were treated using focused ultrasound for the purpose of triggering inflammation-induced anti-tumor immunity, and *in vivo* BLI was used to monitor changes in local and systemic NF-κB activation.

Methods

Generation of Novel PyNGL Murine Model

An F1 breeding strategy was implemented to create the PyNGL murine model. Both MMTV-PyMT tumor and NGL luciferase genes are dominant, so MMTV-PyMT positive males were bred with homozygous NGL positive females. With this breeding strategy, 100% of offspring were heterozygous for the NGL trait, approximately 50% were heterozygous for the MMTV-PyMT trait (assume trait is evenly distributed between genders), and 50% of offspring will be female; this resulted in 25% of total offspring that were females with PyMT and NGL genetics. The use of homozygous NGL female breeders allowed this double-transgenic strategy to maintain the same efficiency of target offspring production as single-transgenic PyMT breeding.

Bioluminescent in vivo *Imaging*

At least 24 hours prior to imaging, an electric razor was used to shave the anterior surface of the mouse including the thorax and abdomen, and then a depilatory cream (Nair, Church & Dwight Co., Inc., Ewing, NJ) was applied for 90 seconds to the shaved region before removal with water. An *In Vivo* Imaging System (IVIS) Lumina Series III (Caliper Life Sciences, PerkinElmer acquisition, Waltham, MA) was used to measure bioluminescence in PyNGL mice following intraperitoneal injection of 0.1 mL luciferin D-firefly in PBS (10 mg/mL; Biosynth L-8240). Images were acquired with 7-second exposure, unless otherwise noted, and a sequence setup was used to acquire one image every minute for 40 minutes. During each session, 1-3 mice were placed on the IVIS platform for imaging of the flank or tumors. The mice were placed either: 1) prone for flank imaging of NGL mice, or 2) supine for tumor imaging of PyNGL mice with the paws loosely taped to the IVIS platform to expose the anterior surface during imaging. Prior to treatment (FUS or no treatment), 1-3 baseline (pre-treatment) IVIS time points were collected; for both untreated and FUS-treated mice, this timing was determined by size of the largest tumor, selected for a maximal dimension of 1-1.5 cm. Mice were imaged at multiple time points after treatment, with a minimum of 12 hours between IVIS imaging sessions for up to 6 days, followed by up to 4 imaging sessions per week, at least 24 hours apart, until euthanasia. Mice underwent a maximum of 20 total IVIS imaging sessions.

IVIS Image Processing Technique

Regions of interest (ROIs) were defined for each mouse to include the head (R_1 – Figure 3) and two mammary tumors (R_2 and R_3 – Figure 3). These ROIs were placed on each sequential image (S_i – Figure 3) within a time point (T_j – Figure 3). Adjustments were made for placement of ROIs between time-point imaging sessions of a particular mouse, such that anatomical localization was maintained, despite minor variations in subject placement. Average radiance was measured in the ROIs for every image within each

imaging session and at all time points. Within each time point, the maximum value of average radiance was selected for each R (Figure 3A); this can be thought of as the "true average radiance," as it accounts for timing variations in delivery and metabolism of luciferin, which may result from factors including altered tumor vascularization[127,128] and luciferin dosage[127] (see Figure 7 for empirical support). A two-step normalization process (Figure 3B) was then used to measure ROI radiance with respect to baseline and account for day-to-day variations in signal due to stress or other systemic factors. This two-step process (Figure 3) includes 1) normalization of ROIs in each time-point to their respective baseline time-point values, then 2) normalization within each time-point of the tumor ROIs to the head ROI. Generally, step one sets up the framework for BLI analyses to assess response as a relative change from baseline, while step two accounts for day-to-day systemic luminescence variations due to luciferin injections and stress-induced NF-κB activity. The ubiquitous nature of NF-κB throughout the body, and the particularly high background activity levels in tumors, necessitated BLI quantification methods with high sensitivity. This need was realized with the use of true average radiance within each time-point ROI and the implementation of a two-step normalization process.

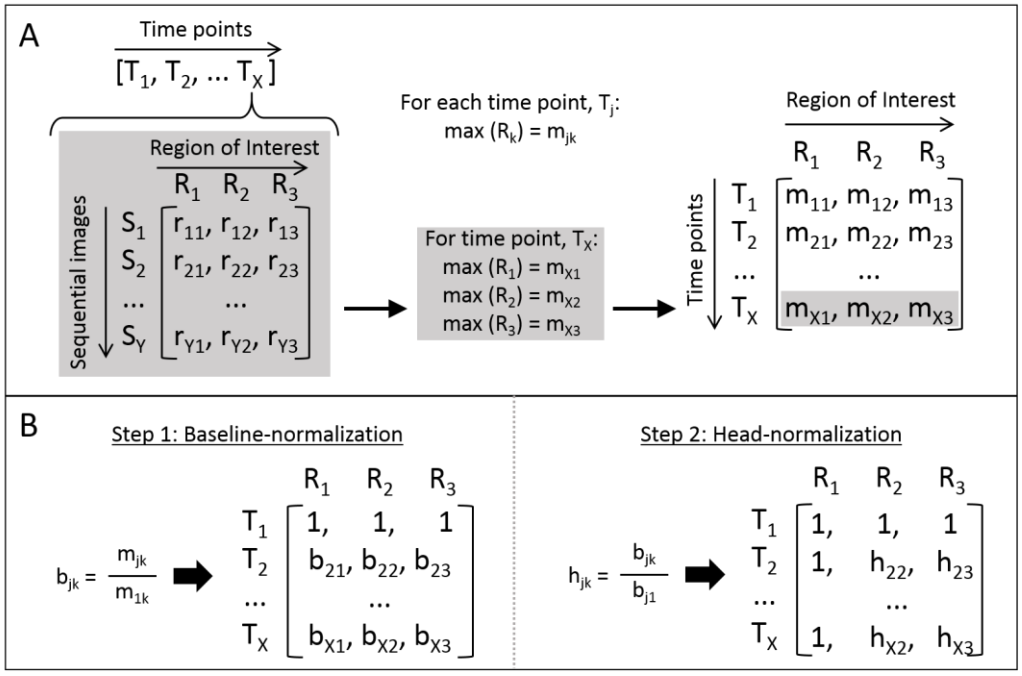

Figure 3. ROI analysis and normalization process. (A) For every time point, $T_{(1:X)}$, there are a sequence of 40 images, $S_{(1:Y)}$, where a delay of 60 seconds separates sequential images. Within each image, there are 3 regions of interest selected for analysis: R_1 is the head, R_2 is one tumor, and R_3 is a second tumor. Within each time point T_j, the value of each region of interest R_k is determined for all S_i as r_{ik}. For T_j, the maximum value of $r_{(1:Y)k}$ for each R_k is identified as m_{jk}. (B) A two-step normalization process of the m_{jk} matrix is used. First, each R is normalized by dividing each time point by the initial time point (T_1), resulting in a new matrix of baseline-normalized values, b_{jk}. Baseline-normalization allows data from each time point to be assessed as a change relative to background activity. Next, head-normalization is done, such that R_k is divided by R_1 within each time point for an h_{jk} matrix. Head-normalization accounts for day-to-day variables such as injected luciferin amount and systemic NF-κB changes.

Therapeutic Focused Ultrasound

Focused ultrasound (FUS) was used to deposit either thermal or mechanical energy into the tissue. A waveform generator (Agilent 33511B, Agilent, Santa Clara, CA USA) and radio frequency amplifier (E&I A150, Electronics & Innovation, Ltd. Rochester, NY USA) were used to create the ultrasound signal, which was then focused by the FUS transducer (H-101MR single element, 1.1 and 3.3 MHz operation, 400W, Sonic Concepts, Bothell, WA, USA). The transducer was fixed into place at the base of an open-tipped plastic cone, which was subsequently filled with vacuum-degassed water. An acoustically transparent

latex membrane sealed the open tip of the cone, and ultrasound gel was used to couple the cone to mice, such that it was in contact with the skin over the tissue to be treated.

Thermal FUS was guided with a closed-loop feedback system, employing magnetic resonance-thermometry (MRT) to monitor and control thermal dosing in real-time (Figure 4). Detailed in Poorman et al,[129] during hyperthermia FUS (hFUS) treatment, the murine subject was affixed to a platform with the tissue of interest placed on the treatment surface of the ultrasound transducer cone. A heated-water pad was positioned between the mouse and platform to maintain body temperature, and inhaled isoflurane anesthesia was maintained via breathing tube and nose cone. During treatment, constant surveillance of temperature and respiratory rate were monitored with a rectal thermometer and an attached respiratory monitor pad, respectively. The entire treatment platform was placed into a Varian 4.7T magnetic resonance imaging system for treatment. Output voltage of the waveform generator was determined by the real-time feedback loop, to achieve and maintain a 6 °C change in temperature from baseline. An output voltage limit was set for 70 mV, corresponding to approximately 1.5 MPa peak negative pressure, to minimize cavitation activity.

Mechanical FUS (mFUS) treatment employed the same treatment platform used for hFUS, but treatments were conducted on a benchtop, without MR imaging. Mice were similarly anesthetized, however, no heated-water pad, breathing monitor, or thermometer were required. Sonication was conducted at the 1st harmonic (center frequency of 1.1 MHz) with either high level mFUS (mFUS-high) or low level mFUS (mFUS-low). The peak negative pressure (PNP) induced by sonication is related to the amplitude of voltage used. A calibration curve was generated measuring the pressure changes in a phantom at specific voltages to generate a linear regression; however, the relationship is non-linear at high driving voltages. For this reason, the PNP values of the two mFUS treatment levels were calculated with the linear regression and adjusted by a factor of approximately 0.75 for low mFUS and 0.65 for high mFUS, similar to the work done by Maxwell et al[130]. High level mFUS was done using an 8.5 MPa PNP burst

with a period of 20.00 msec, and 22 kilocycles for five applications of 60 seconds with a repetition frequency of 1 Hz. After each 60-second application, the transducer was moved slightly to treat have a different focal point within the same tumor. Low level mFUS was done using an 8 MPa PNP burst with a period of 1 msec, and 1100 cycles for one application of 30-60 sec with a repetition frequency of 1 Hz.

Preliminary trials of hFUS were conducted in the flank of NGL-only mice to verify that FUS-induced changes in NF-κB activity would be observed and detectible by IVIS. PyNGL tumor experiments were performed with FUS treatment of a single primary tumor per treated mouse. Mice received FUS when the tumor to be treated reached a diameter of at least 1 cm.

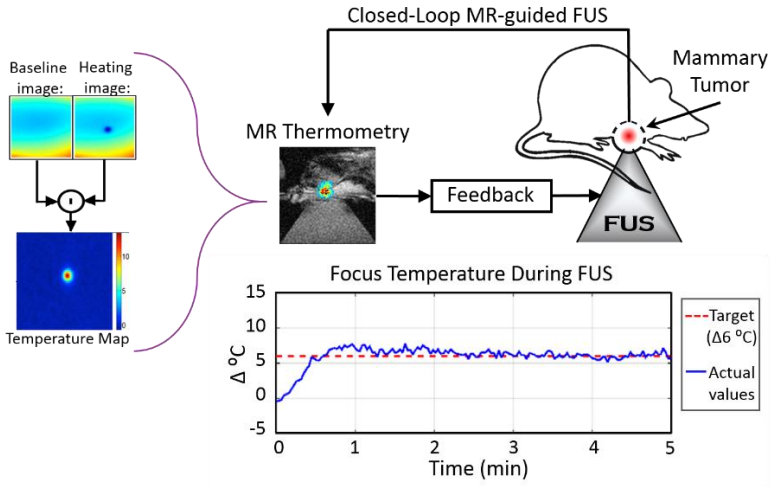

Figure 4. MR-guided FUS feedback loop for controlled hFUS treatment. For treatment, the mouse (specifically the tumor) is placed onto the FUS transducer, then the mouse and transducer are placed into the bore of a 4.7T MR imaging system. MR thermometry is used to monitor and control thermal dosing. MRT is based on the way protons act in a magnetic field[51], which is dependent on a known relationship with temperature, so MR images are taken prior, and throughout, ultrasound treatment. With each subsequent image, the baseline activity image is subtracted in real time to create a temperature map. Using this map, temperature at the focal spot in the tissue can be quantitatively traced during treatment. A target temperature of Δ6 °C is set for the focal spot and used in conjunction with the temperature map to turn the ultrasound on and off as needed to reach and maintain target heating. There is an initial lag time during which energy deposition into the tumor ramps up to reach this target temperature, then the feedback system allows automatic maintenance of this temperature in the tumor tissue throughout the treatment, 5 minutes of which is shown in the Focus Temperature graph.

Tissue Collection

At 48 hours post-treatment mice were euthanized and tissues collected into ice-cold DPBS (Dulbecco's Phosphate Buffered Saline, 1X without calcium & magnesium). For untreated mice, this time point was selected based on when the mouse would have been treated according to tumor size (described above in *Bioluminescent* in vivo *Imaging*). A portion of each collected tumor was stored in 10% formalin (4% Formaldehyde Solution, Fisher Scientific) for tissue fixation. In treated mice, the mechanically treated tumor (MTT), an untreated tumor within the treated mice (contralateral tumor (CLT)), and the spleen were collected. In untreated mice, one or more untreated tumors (UTTs) were collected, including the largest tumor for similarity to MTTs, as well as the spleen. Tissues were mechanically dissociated with a straight razor blade and subsequently filtered through 70 μm nylon mesh filters (Fisher Scientific, Pittsburgh, PA). The resulting cell suspensions were centrifuged, supernatant collected and frozen at -20 °C, and pellets resuspended in 1 mL ACK lysing buffer (KD Medical Inc., Columbia, MD) for 2 minutes before dilution with 20 mL ice-cold DPBS. Suspensions were centrifuged again, supernatant aspirated away, and pellets resuspended in 600 μL DNase (DNase I, RNase-free, BioRiad, Hercules, CA) in HBSS (Hanks' Balanced Salt Solution, 1X with calcium and magnesium). The DNase-cell suspension was kept at room temperature for 30 minutes and diluted with ice-cold DPBS. After a final centrifuge step, supernatant was aspirated away, and pellets were resuspended in 2 mL of 90% FBS with 10% DMSO. The final cell suspension was aliquoted into cryovials and frozen. Cryovials were cooled at a rate of -1 °C/minute to -80 °C before transfer to liquid nitrogen. All centrifuge steps were conducted at 200 xg for 10 minutes at 4 °C.

Flow Cytometry

Cells were rapidly thawed from liquid nitrogen, resuspended in 10 mL ice-cold DPBS, centrifuged, and the pellets resuspended into ice-cold DPBS. Cells were stained with the following rat anti-mouse antibody-fluorochrome conjugates: 1 μg/10^6 cells of CD3-AlexaFluor 700 (clone 17A2, BD Biosciences, San

Jose, CA), 0.09 µg/10^6 cells of CD4-FITC (clone RM4-4, BD Biosciences, San Jose, CA), and 0.01 µg/10^6 cells of CD8b-PE (clone H35-17.2, BD Biosciences, San Jose, CA). After incubation with the antibodies for 30 minutes at room temperature, cells were washed twice with DPBS, and resuspended in 2 mL 75% methanol in DPBS with 1.2 µg/10^6 cells Hoechst (Hoechst 33342, trihydrochloride, trihydrate, 10 mg/mL solution in water, Life Technologies) for 30 minutes at room temperature. Cells were centrifuged at 900 x g for 15 minutes at 4 °C, resuspended in 500 µL DPBS, and analyzed with a BD LSRFortessa (Beckton-Dickson, San Jose, CA USA) flow cytometer.

Flow Cytometry Gating

The gating strategy employed (Figure 5) was used for doublet elimination, selection of DNA-containing cells, lymphocyte gating, and T cell isolation and phenotyping. Side scatter (SSC), a measure of cell granularity[131], was used to eliminate doublets based on the approximation of a 1:1 ratio for SSC-area (SSC-A) and SSC-height (SSC-h) expected for single cells. Forward scatter (FSC), a measure of cell size[131], was similarly used to eliminate doublets by the expected 1:1 ratio of FSC-area (FSC-A) and FSC-height (FSC-H) expected for single cells. Following doublet elimination, single cells are identified by positive Hoechst staining for the presence of DNA, eliminating debris aggregates. Lymphocytes are identified by the known relationship between their size and granularity[132,133], and T cells are then selected by the presence of CD3+ (general T cell marker). T cells are then further classified by the presence of either CD4+ (helper and regulatory T cells) or CD8+ (cytotoxic T cells).

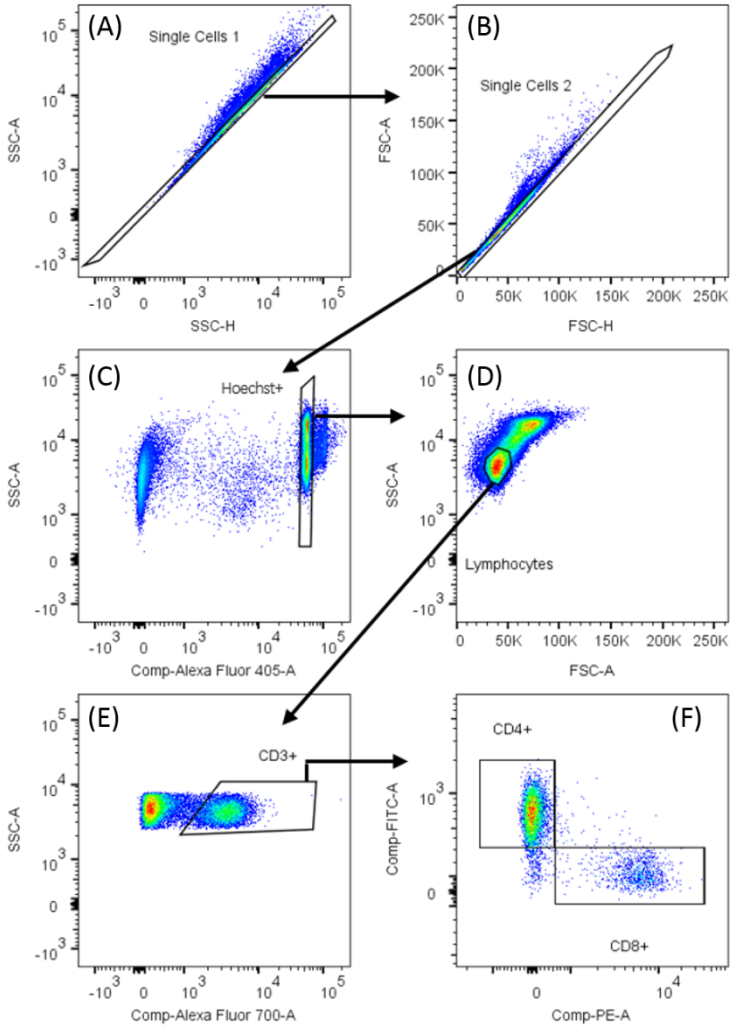

Figure 5. The flow cytometry data shown, from the spleen of a mouse treated with mFUS, is representative of the gating process used to analyze tissues from 14 mice. Single cells were isolated by: (A) doublet exclusion by SSC-A: SSC-H ratio, (B) doublet exclusion by FSC-A : FSC-H ratio, and (C) uniform DNA content determined by Hoechst+. (D) Lymphocytes were isolated with standard SSC-A versus FSC-A gating for size and granularity[131]. (E) T cells were selected based on CD3+ staining, and (F) were subsequently phenotyped based on either CD4+ or CD8+ staining.

Immunohistochemistry

Tumor portions that were formalin-fixed at the time of tissue collection were subsequently processed in the Vanderbilt Translational Pathology Shared Resource (TPSR). Tissues were paraffin-embedded and sectioned with 5-µm thickness. From each tumor, a minimum of two sections were obtained and mounted on separate slides. One section was stained with hematoxylin & eosin. For

immunohistochemistry staining of the two other mounted tissue sections, slides were placed on the Leica Bond Max IHC stainer. All steps besides dehydration, clearing and coverslipping are performed on the Bond Max. Slides are deparaffinized. Heat induced antigen retrieval was performed on the Bond Max using their Epitope Retrieval 2 solution for 20 minutes. One slide per tissue was incubated with anti-Foxp3 (Cat#13-5773-82, eBioscience, Inc., San Diego, CA) for one hour at a 1:100 dilution and followed by a biotinylated anti-rat (Cat#BA-4000, Vector Laboratories, Inc., Burlingame, CA) for 15 minutes at a 1:200 dilution. The Bond Polymer Refine Detection system (Cat#DS9800, Leica Biosystems, Newcastle Upon Tyne, United Kingdom) was used for visualization. The other slide for each tissue was then incubated with anti-CD4 (Cat#14-9766-80, eBioscience Inc, San Diego, CA) for one hour at a 1:1000 dilution and then incubated in a rabbit anti-rat secondary (BA-4001, Vector Laboratories, Inc.) for 15 mins at a 1:200 dilution. The Bond Polymer Refine Red Detection system (Cat#DS9390, Leica Biosystems, Newcastle Upon Tyne, United Kingdom) was used for visualization. Slides were then dehydrated, cleared and coverslipped.

Slides were imaged at the Vanderbilt Digital Histology Shared Resource using the Leica SCN400 Slide Scanner (Leica Microsystems Inc., Buffalo Grove, IL) and image analyses were conducted using the Digital Image Hub (Leica Biosystems, Nussloch, Germany). Separate slides from each tissue section imaged following staining for CD4 or FoxP3, with CD4+ stained cells including both T_{helper} and T_{reg} cells. FoxP3 staining was used to identify T_{reg} (FoxP3+) cells and calculate the percent of CD4+ cells which were T_{reg} and T_{helper}. Multiple location-matched regions of interest were selected on both stained slides from each tissue. Within corresponding ROIs, the number of CD4+ or FoxP3+ stained cells, respectively, were counted and taken as a percent of total cells within the region of interest. The percent of CD4+ T cells of the Treg phenotype was calculated as the ratio of % of cells FoxP3+ cells divided by % of cells CD4+; the remainder of CD4+ cells were identified as T_{helper} cells.

Cytokine Analysis by Flow Cytometry

The supernatant collected and frozen during tissue processing was used to assess relative expression of cytokine levels. We designed a multiplexed cytometric bead array, selecting combinable kits from the enhanced sensitivity (ES) flexible set options (BD Biosciences, San Jose, CA) to measure IL-6, IL-2, IL-10, IL-17a, TNF-α, and IL-1β. The kit includes known lyophilized amounts of the selected cytokines (standards), wash buffer, mouse detection reagent (antibody), enhanced sensitivity detection reagent (fluorescent antibody), and capture beads, which are microscopic beads coated with antibodies for a specific cytokine. All of the ES capture beads have varying levels of two fluorophores (APC and APC-Cy7). The relative intensities of bead fluorescence relative to the other beads in the set allows multiple cytokine capture beads to be used in conjunction for multiplexed analysis of a single sample. The detailed protocol is available through the BD Biosciences website[134]. Briefly, capture beads for the six selected cytokines were mixed in equal parts. Standards were mixed in equal parts for each cytokine, and then serially diluted for solutions with known cytokine concentrations. The frozen supernatants were thawed and 25 µL of each were placed into separate tubes. The ES capture bead mixture was added to each sample and standard tube and allowed to incubate for 2 hours at room temperature. Mouse detection reagent was added to each tube and incubated for an additional 2 hours. The mouse detection reagent is an antibody specific to the mouse Fc-region. The samples were washed, resuspended with enhanced sensitivity detection reagent, and incubated for 1 hour. Similarly, the enhanced sensitivity detection reagent is a fluorescent antibody specific to the Fc-region of the mouse detection reagent. The samples were then washed, resuspended in wash buffer, and analyzed on a BD LSRFortessa (Beckton-Dickson, San Jose, CA USA) flow cytometer.

Statistical Analysis

Statistical analyses were conducted with GraphPad Prism (GraphPad Software, Inc., La Jolla, CA). The Mann-Whitney test was used to determine statistical significance, with $p < 0.05$.

Results and Discussion

FUS Generates Measurable NF-κB Changes in NGL Mouse Flank

Prior to breeding the double-transgenic PyNGL model, a preliminary study was conducted using FUS therapy in the flank of a non-tumor bearing NGL mouse. IVIS data was collected and processed as described, with regions of interest for the head (R1), an untreated area of the flank (R2), and the hFUS treated area of the flank (R3), to characterize changes in NF-κB pathway activity. Figure 6 shows IVIS images at 0 and 48 hour time points for two mice, where Mouse α was treated on its right flank with hFUS at Δ6 °C for 10 minutes, while Mouse β was untreated. The processed radiance data (Figure 3) suggests FUS treatment induced a change in NF-κB activity in treatment-localized tissue.

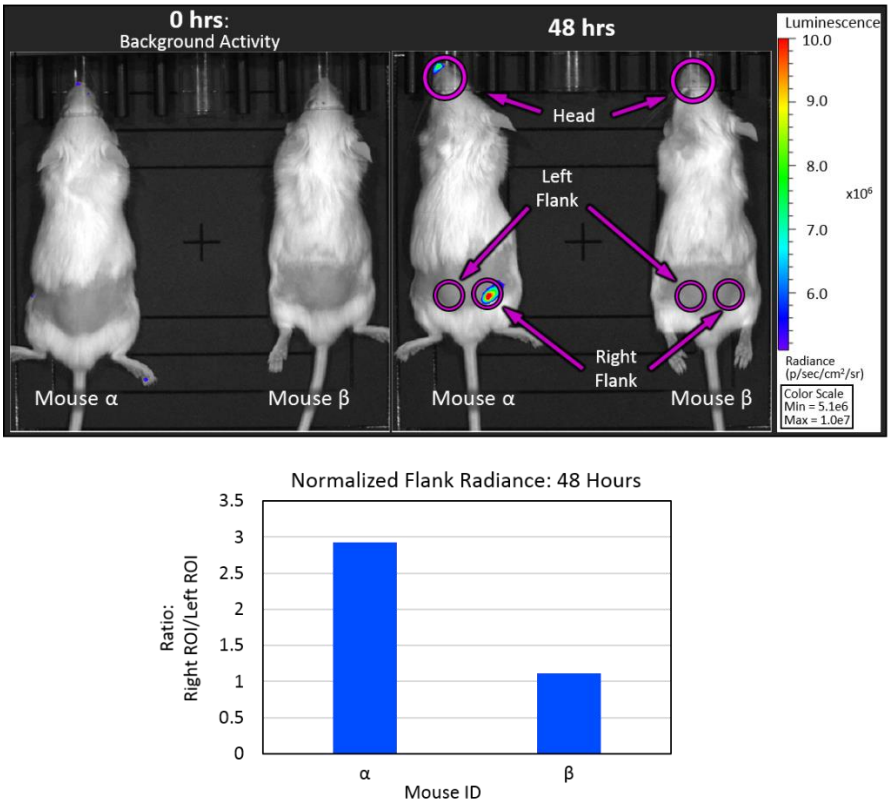

Figure 6. NGL mice were imaged with IVIS prior to treatment and 48 hours after treatment. Image exposure settings were automatically determined by the imaging software. Mouse α was treated with hFUS on the right flank and Mouse β was untreated. The graph shows a ratio of right flank ROI normalized radiance to left flank ROI normalized radiance. While the ratio of right to left flank in Mouse β is roughly 1, the ratio for Mouse α is approximately 3. This indicates that, following treatment, the treated right flank of Mouse α has nearly 3 times more NF-κB activity. For this preliminary flank study, n = 1 for hFUS and n = 1 for no treatment, therefore no statistical analyses were conducted.

Sequence Imaging is Necessary for ROI Maximum Radiance

Initial studies suggested variation in the biodistribution of intraperitoneally injected luciferin. Contralateral tumor radiance for an imaging sequence at a single, pre-treatment time point is shown for four mice in Figure 7A. The trajectory of sequence radiance approximates a logarithmic curve, and the maximum value is reached at different times following injection. Figure 7B shows the percent error that would occur if a single measurement were taken at 16 minutes after injection. These variations may be

attributed to biological variability between mice, tumor vasculature, or IP injection. Sequence imaging ensures maximum values can be measured and normalized for comparison between time points.

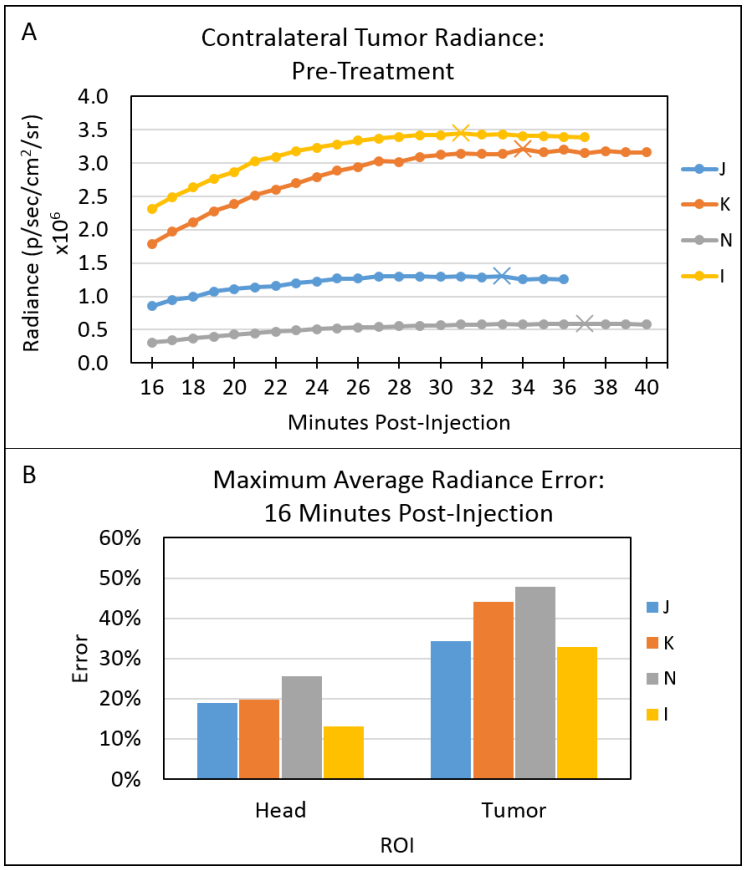

Figure 7. Following luciferin injection, a sequence of IVIS images were collected, with a delay of 60 seconds between consecutive images. Image exposure settings were automatically determined by the imaging software. A) Plot of CLT radiance over the sequence of images collected at one pre-treatment time point for 4 mice (J, K, N, and I). The maximum radiance value, indicated on each data set by "X", ranges in magnitude and time to occurrence following injection. B) Sequence radiance of the ROI for the mice and time points in (A) was used to calculate percent error comparing maximum ROI radiance to ROI radiance at 16 minutes after injection. The two-step normalization process was not used for single time point analysis.

NF-κB BLI Indicates Temporal Changes of Response to Treatment

Successful cross breeding of the PyMT and NGL models resulted in the generation of the PyNGL double-transgenic mouse model, as verified by tail-cut genotyping for the presence of GFP and PyMT transgenes (Transnetyx, Inc., Cordova, TN). The first hFUS treated PyNGL mouse was imaged with IVIS for 2.5 weeks following treatment. Using this IVIS data (Figure 8), the radiance, linked to NF-κB activity levels, in the hyperthermia-treated tumor (HTT) decreased to approximately 50% of baseline values at 48 hours and stayed below baseline for the remaining time points, suggesting a change in NF-κB activity, potentially as a result of FUS treatment. The primary focus of the completed studies was to characterize early adaptive response in FUS-treated tumors (HTTs and MTTs). Based on this time course information (Figure 8), the maximum change from baseline in the HTT occurred at 48 hours, therefore tissue collection from subsequent mice was done at 48 hours following treatment. In untreated animals, the baseline and 48-hour time-points were selected based on when the animals would have been treated according to tumor size.

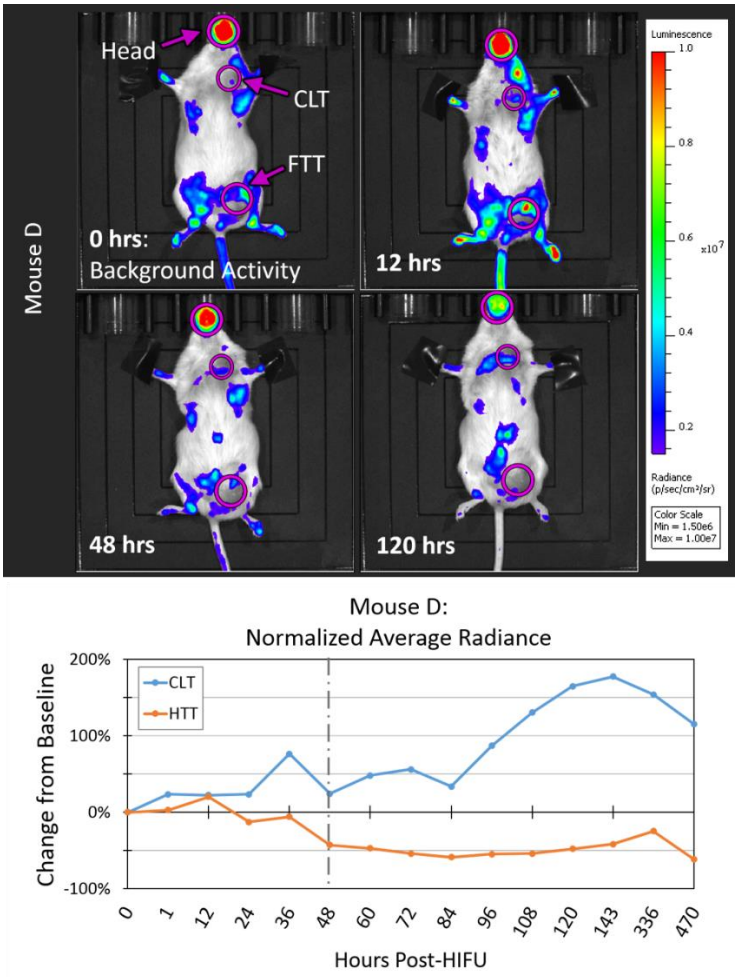

Figure 8. *In vivo* BLI images are taken before and after treatment. Image exposure settings were automatically determined by the imaging software. This figure is a representative example (1 hFUS-treated mouse) of IVIS images and trajectory. IVIS images shown were taken at 0 hours, to measure background NF-κB activity prior to treatment, and at 12, 48, and 120 hours following treatment. Purple circles denote the three defined regions of interest: head, contralateral tumor (CLT), and hyperthermia-treated tumor (HTT). Baseline NF-κB activity at 0 hours is noted primarily in the head, mammary glands, and regions of exposed skin, such as the tail and paws. The normalized radiance data for CLT and HTT is plotted. At 12 hours, both CLT and HTT have increased slightly from baseline. By 48 hours, HTT has decreased to approximately 50% of baseline activity, which is maintained through 470 hours. In contrast, CLT increased more than 150% from baseline, reaching a peak at 143 hours before trending back towards baseline activity level. A total of 2 mice were analyzed in this way to establish the most appropriate time for subsequent analyses.

Similarly, mice treated with mFUS were imaged every 12 hours for 48 hours following treatment to identify time-course changes in radiance. Figure 9 depicts the change in normalized tumor radiance for untreated and mFUS-treated mice. From Figure 9.A, both the average MTT and CLT-M (contralateral

tumors from mFUS-treated mice) normalized radiance values increase from baseline to 48 hours. This shows a change that occurs in NF-κB activity by 48 hours, supportive of the decision to collect tissues 48 hours after treatment. While Figure 9.A depicts averages with standard error for UTTs, MTTs, and CLT-Ms, Figure 9.B shows individual measurements for MTTs and representative UTTs. At 48 hours post-treatment, two MTTs exhibit an increase from baseline of approximately 200% (Figure 9.B). This change in normalized average radiance is distinctly different from the response observed in the UTTs and in the other three MTTs. Additionally, normalized average radiance at the 12 hour time point did not predict for response at 48 hours. This indicates that the time course and level of NF-κB response varies between animals, potentially arising from variations in pre-treatment tumor microenvironment. Statistical analysis of this data is shown in Figure 10, along with IVIS data from an additional treatment group.

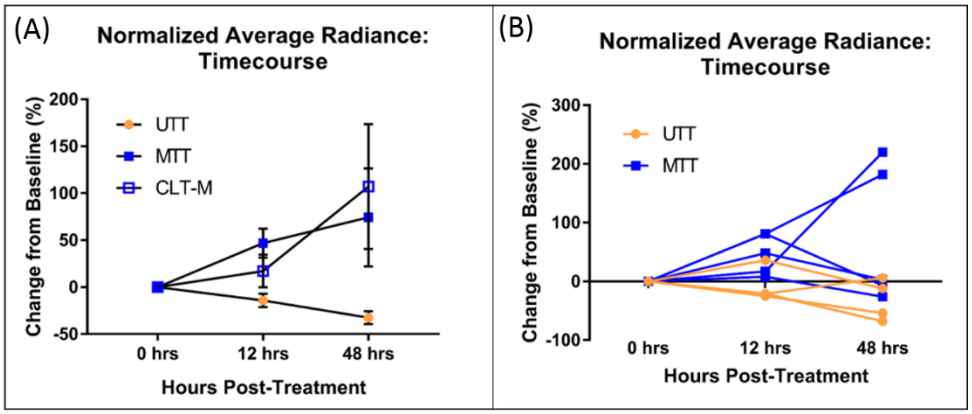

Figure 9. Normalized radiance, shown as relative change from baseline. (A) Time course of aggregate data plotted as mean with standard error, includes UTT, MTT, and CLT for mFUS (CLT-M). (B) Time course for individual mice: 5 MTTs and 4 UTTs. One untreated mouse was imaged with exposure settings automatically determined by the imaging software. Error bars show standard error for each tissue and time point.

BLI Indicates Treatment-Response Relationship

Tumors from PyNGL mice were treated with FUS or no treatment and subsequently imaged with IVIS. Figure 10 depicts the normalized IVIS data at 48 hours after treatment from 5 mFUS-treated mice, 6 hFUS-treated mice, and 4 untreated mice. In each untreated control mouse, four UTT's were selected to account for inter-mouse variability. At the 48-hour time point, a statistically significant increase in radiance was observed in MTTs as compared to UTTs, demonstrating a direct effect of mFUS on tumor NF-κB activation levels. Furthermore, contralateral tumors in mFUS-treated mice (CLT-Ms) exhibit a similar response, with a statistically significant increase compared to UTTs. The response detected in distant, untreated tumors (CLT-Ms) suggests that, in addition to the direct effect of mFUS on the treated tumor, mFUS is also capable of generating a distant response. Large variability is seen in mFUS treated tumor measures, with two subjects having experimental values for both MTT and CLT-M exhibiting a change from baseline ranging from 180-270%. These two experimental subjects cause the statistical significance seen between UTTs and MTTs or CLT-Ms, suggesting a subset of mice which may have a more substantial NF-κB response to mFUS treatment. In contrast, no statistical difference was observed between HTTs and UTTs; however, CLT-Hs did exhibit a statistically significant increase over UTTs, indicating that, while no direct effect on HTTs was observed, a remote effect was generated. The reporter model provides a basis for relating radiance to activation of the NF-κB pathway. Increased radiance observed in MTTs but not HTTs, as compared to UTTs, supports the idea that mFUS and hFUS operate by different mechanisms of action[60]. The remote response in CLT-Ms and CLT-Hs suggests that both mFUS and hFUS have the potential to induce a systemic, abscopal effect.

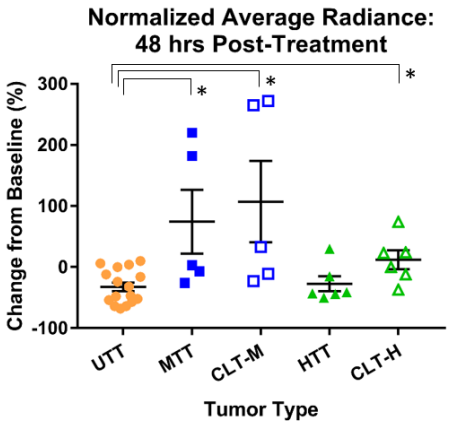

Figure 10. Normalized IVIS data for 15 PyNGL mice 48 hours after treatment. Treatment groups include 5 mFUS-treated mice (MTT & CLT-M), 6 hFUS-treated mice (HTT & CLT-H), and 4 untreated mice (UTT). Displayed, 4 UTTs were included per untreated mouse for a total of 16 UTT values. One untreated mouse and all hFUS treated mice were imaged with exposure settings automatically determined by the imaging software. Mean and standard error are shown in black for each ROI. The two-tailed Mann-Whitney test was used to assess statistical significance. The pairs: MTT – UTT, CLT-M – UTT, and CLT-H – UTT had values of $*p < 0.05$. All other pair-wise analyses had values of $p > 0.05$.

While Figures 9 and 10 present data for a single CLT-M from each mFUS treated mouse, the spontaneous model develops multiple fat pad tumors. Figure 11 shows normalized average radiance where four tumors were included per mouse – four UTTs per untreated mouse, and one MTT with three CLT-Ms per mFUS treated mouse. Statistical significance is maintained between UTTs and CLT-Ms when multiple CLT-Ms are included per mouse, while no significant difference exists between CLT-Ms and MTTs. This confirms that the mFUS-induced change in radiance is systemic, further supporting a potential abscopal effect.

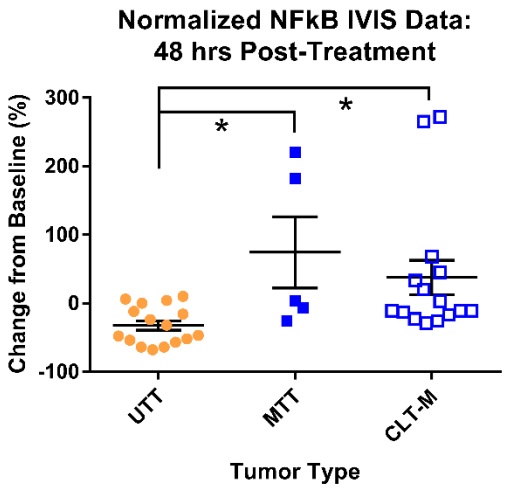

Figure 11. Normalized IVIS data for 9 PyNGL mice 48 hours after treatment. Treatment groups include 5 mFUS-treated mice (MTT & CLT-M) and 4 untreated mice (UTT). Displayed, 4 UTTs were included per untreated mouse for a total of 16 UTT values and 3 CLT-Ms were included per mFUS treated mouse for a total of 15 CLT-M values. One untreated mouse was imaged with exposure settings automatically determined by the imaging software. Mean and standard error are shown in black for each ROI. The two-tailed Mann-Whitney test was used to assess statistical significance. The pairs: MTT – UTT and CLT-M – UTT had values of $*p < 0.05$, while MTT – CLT-M had a values of $p > 0.05$.

Flow Cytometry Indicates T Lymphocyte Shift

Quantitative analysis of flow cytometry data (Figure 12) reveals significant differences in immune cell populations among treated and untreated tissues. Initially, group analyses were conducted in a binary manner, such that mice were either untreated or mFUS-treated. Binary group analysis of flow cytometry data revealed a larger range of values for MTTs than for UTTs, suggesting that mFUS treatment may induce a more significant immune response in a subset of treated animals. Consequently, mFUS-treated mice were further classified as responders or non-responders to mFUS treatment, selected for highest percent of CD3+ T cells in the spleen. This criteria was selected based on the critical role of the spleen as a secondary lymphoid organ, where antigen presenting cells and adaptive immune cells accumulate from circulation[135,136]. The dense presence of both cell types provides an environment suitable for antigen presentation and cross-presentation to lymphocytes. Categorization of mFUS-treated mice into responder and non-responder groups is based on the understanding that the efficacy of a given immunotherapy

varies widely among patients; while some patients may experience complete remission, others may have no response. Separation of responders from non-responders allowed extrication of treatment-induced effects in mice receptive to mFUS-induced immunological changes.

Previous studies have demonstrated that an increased CD4+/CD8+ ratio is associated with improved outcomes[90], and can be generated in tumors with FUS treatment[97]. The CD4+/CD8+ T cell ratio in tissues of untreated mice was not statistically different from that of mFUS-treated mice (Figure 12.A); however, analysis of the CD4+/CD8+ ratio for mFUS-treated mice considered separately as responders (Figure 12.B) and non-responders (Figure 12.C) revealed significant difference in the ratio between responder MTTs and UTTs. Similarly, the percent of T cells which were CD4+ in responder MTTs was statistically higher than UTTs (Figure 12.E), while no statistical difference from UTTs was observed for combined MTTs (Figure 12.D) or non-responder MTTs (Figure 12.F). Interestingly, the percent of CD4+ T cells, when comparing spleens of treated mice (SPL-Tr) to spleens of untreated mice (SPL-Un), is statistically higher for combined SPL-Tr (Figure 12.D) and non-responder SPL-Tr (Figure 12.F), but not for responder SPL-Tr (Figure 12.E). The percent of T cells which were CD8+ in tissues of untreated mice was not statistically different from those of treated mice, whether considering combined mFUS-treated mice (Figure 12.G), responders (Figure 12.H), or non-responders (Figure 12.I). Together these data suggest that, in the responder subset of mFUS-treated mice, a change was induced in the T cell profile. Additionally, the increased CD4+ T cells in the spleens of non-responders may indicate potential for an immunological change in these mice. The non-responders may have different response kinetics with CD4+ T cells still undergoing proliferation in the spleen, or these animals may be undergoing an alternate type of immune response.

The 48 hour time-point was selected based on pilot mice following FUS treatment-modulated NF-κB activation. It is possible that immune cell response to FUS lags NF-κB activation resulting in the observed variability of T cell response at 48 hours. Longer post-treatment observation times may provide

a more comprehensive view of T cell infiltration and impact on tumor burden, as well as insight into the differences between responders and non-responders.

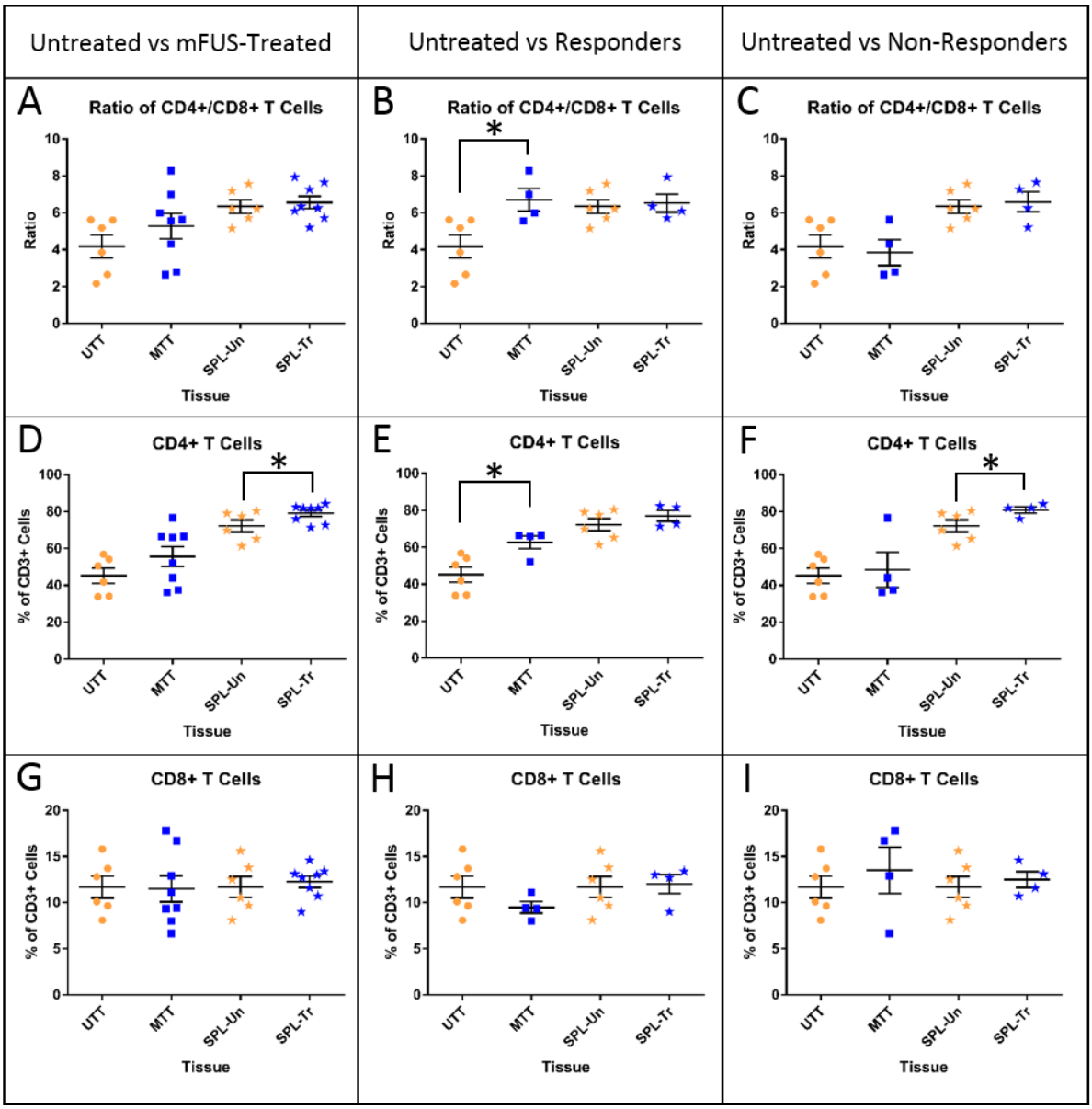

Figure 12. Quantified flow cytometry data are shown from untreated tumors (UTTs), mFUS-treated tumors (MTTs), and spleens from the corresponding untreated and mFUS-treated mice (SPL-Un and SPL-Tr, respectively). Using the described gating strategy, T cells (CD3+) were phenotyped based on expression of either CD4+ or CD8+ markers. In addition to the percent of T cells which were CD4+ or CD8+, the ratio of CD4+/CD8+ T cells was also assessed. For all three measures, the range of MTT values exceeded that of UTT, leading to subclassification of mFUS-treated mice into two response categories: responders and non-responders. Results for untreated mice are shown with data for aggregated mFUS-treated mice (left

column), responders (middle column), and non-responders (right column). (A-C) Ratio of T cells which were determined to be CD4+ versus CD8+ (CD4+/CD8+ ratio), shown for (A) aggregated mFUS-treated mice, (B) only responders, and (C) only non-responders. (D-F) Percent of T cells which are CD4+, shown for (D) aggregated mFUS-treated mice, (E) only responders, and (F) only non-responders. (G-I) Percent of T cells which are CD8+, shown for (G) aggregated mFUS-treated mice, (H) only responders, and (I) only non-responders. Mean and standard error are shown in black for each tissue. The one-tailed Mann-Whitney test was used for statistical analysis (*$p < 0.05$).

Histology and IHC

Examination of histology data (Figure 13) reveals a prevalence of hyperchomatism in the UTT (Figure 13.A) and a higher presence of pale eosinophilic staining regions in MTTs (Figure 13.B). This structural information suggests that cell death tends to be largely necrotic in MTTs and apoptotic in UTTs[137]. Necrotic cell death is a better stimulator of adaptive immunity than apoptotic death[138]. Additionally, the MTT exhibits a tortuous morphology not seen in the UTT; this may point to structural changes caused by mFUS treatment.

Representative images of IHC slides are shown for a UTT, stained for all CD4+ T cells (Figure 13.C) and FoxP3+ T_{reg} cells (Figure 13.D). Quantitative analysis of IHC (Figure 13.E) shows a presence of T_{helper} and T_{reg} cells in both MTTs and UTTs, however, the T_{helper}/T_{reg} ratio is statistically increased in MTTs, suggesting a more pro-inflammatory, anti-tumor balance in MTTs than in UTTs.

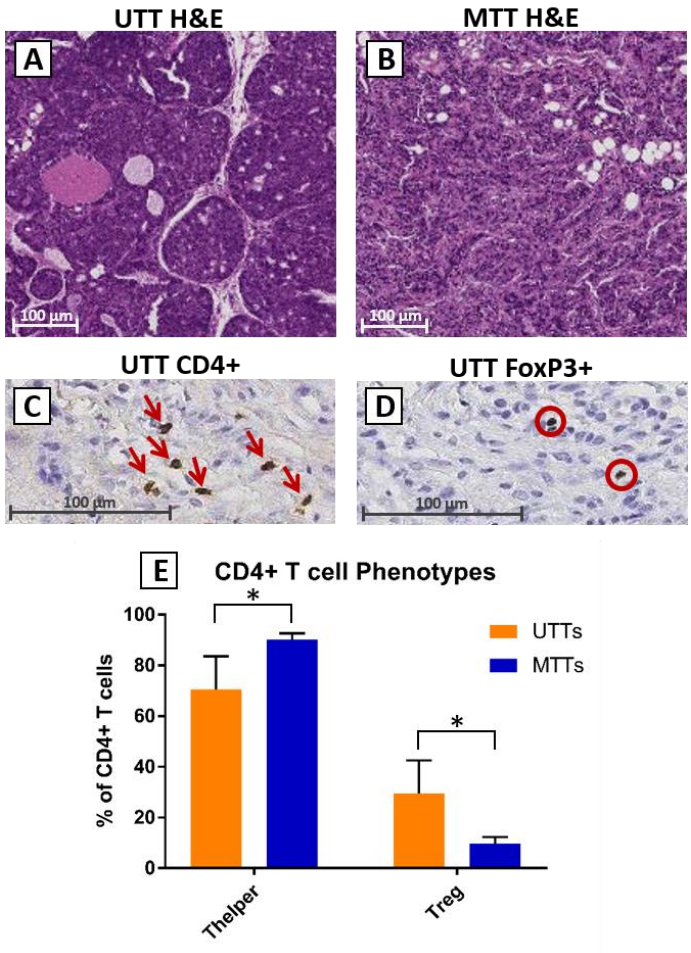

Figure 13. Histology and IHC were used for further characterization of mFUS-induced intratumoral changes. Representative images of H&E, acquired at 4x magnification, are shown for A) a UTT and B) an MTT. Representative IHC images, acquired at 10x magnification, are shown for a UTT stained brown for C) CD4+ T cells [arrows] and D) FoxP3+ T cells [circles]. E) Phenotyping of CD4+ T cells in 4 MTTs and 4 UTTs; the data shows a relative increase in T_{helper} cells and decrease in T_{reg} cells for MTTs compared to UTTs. Mean and standard error are shown. The one-tailed Mann-Whitney test was used for statistical analysis (*$p < 0.05$).

Cytokines

Analysis of cytokine levels in tissues of untreated and mFUS-treated mice (Figure 14) suggests variation. These experimental results were obtained during a pilot run using the BD enhanced sensitivity cytometric bead array. During this trial, IL-1β, IL-2, IL-6, IL-10, IL-17α, and TNF were measured. In the spleens, all six cytokines were present at measurable concentrations; however, in the tumors, the concentrations of IL-2, IL-10, and IL-17α were below the threshold of detection. Figure 14.A shows the

relative level of each of the three detectable cytokines—IL-1β, IL-6, and TNF—cytokine in four tumors (2 UTTs and 2 MTTs) as a percent of the summed concentrations, taken from the same initial volume. Similarly, the level of each cytokine in the corresponding spleens (Figure 14.B) is presented as a percent of the summed concentrations of all six measured cytokines.

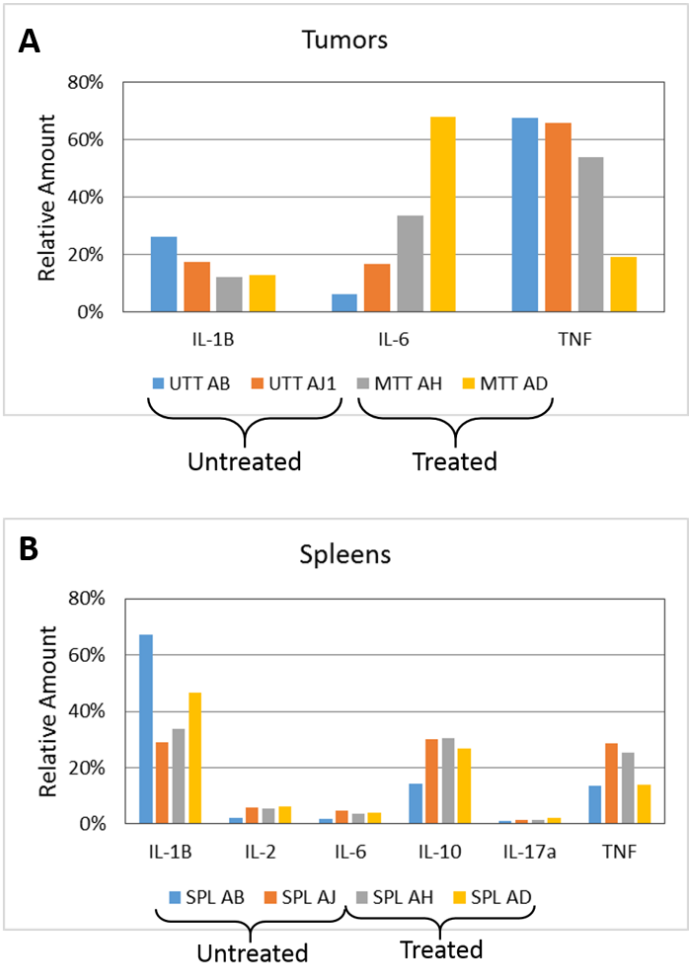

Figure 14. Cytokine measurement results using the enhanced sensitivity CBA kit. Cytokines were measured from tissue digestion supernatants for UTTs, MTTs, and SPLs. Mice AB and AJ were not treated, while mice AH and AD were mFUS-treated. No statistical analysis was conducted due to small sample size.

Conclusion and Future Work

BLI of PyNGL Mice

The novel PyNGL double-transgenic murine reporter model was successfully developed and imaged with BLI for temporal snapshots tracking luminescence-linked NF-κB activation. The ubiquitous nature of NF-κB throughout the PyNGL mice presented a unique window to broadly visualize FUS-induced changes in treated and contralateral tumors but was accompanied by the challenge of resolving treatment-induced changes from background activity. A two-step radiance normalization process was designed and applied, producing results in untreated mice, which were consistent among tumors within each mouse, as well as among mice. This suggests that the normalization process reliably resolves NF-κB-coupled radiance changes within mice, allowing each animal's pre-treatment measurements to function as its own control. Analysis of IVIS measurements using the Mann-Whitney test, suggest that NF-κB activation in MTTs and CLTs for mFUS and hFUS (CLT-M and CLT-H, respectively) are statistically different from UTTs at 48 hours after treatment. The change in radiance for CLTs of both mFUS and hFUS treatments suggests that MTTs and HTTs interact with distant tumors, indicating potential for local and abscopal effects.

Cellular and Molecular Tissue Characterizations

Preliminary assessment of flow cytometry data revealed a larger range of values for MTTs than UTTs, prompting the classification of mFUS-treated mice as responders and non-responders based on the percent of CD3+ cells in the spleen. Flow cytometry results for tumors and spleens of untreated and mFUS treated mice revealed statistically significant differences in the lymphocyte populations. The percent of CD4+ T cells is higher in responder MTTs than in UTTs, as is the CD4+/CD8+ T cell ratio. An increased CD4+/CD8+ ratio has been found to be beneficial in the context of certain types of cancer, and is likely

due to the supportive role that CD4+ T helper cells play in CD8+ T cell effector functions, particularly cytokine moderation of T cell expansion.[139] Our results are consistent with previously reported cavitation[140] and ablation[97] FUS-induced changes. Interestingly, the percent of CD4+ T cells is higher in the spleens of non-responder mice than in untreated mice, suggesting that these mice may have a delayed immune response and still be in the T cell proliferation phase.

Further phenotypic characterization of CD4+ T cells was carried out on tumor sections with IHC, staining for CD4+ and FoxP3+ cell expression. Analysis of IHC sections revealed a higher ratio of T_{helper}/T_{reg}, pointing to a potential mFUS-induced shift from immune suppression towards immune activation. Future work will include immunofluorescence (IF) staining, so multiple markers of interest may be identified on each tissue section. The IF antibody panel will include anti-CD4, anti-FoxP3, anti-CD8, anti-CD45 and anti-GFP, along with markers for nuclei and stroma. These will allow distinction of various T cell phenotypes (CD4, FoxP3, CD8), immune cells (CD45), and NF-κB activation (GFP), while the nuclei and stromal markers provide structural information regarding the localization of immune cells. The CD45/GFP combination will relate NF-κB activation to general cell types to compliment in vivo imaging data with higher specificity. More robust analyses of IHC and subsequent IF are required to verify the initial conclusions.

The TME has a critical, complex role in the therapeutic response to immunotherapy. Cytokines are key moderators of the TME, and preliminary assessment revealed some notable differences, particularly between HTTs and UTTs. The cytokine levels in HTT indicate a potentially significant difference in IL-6 and TNF-α, which suggest some hFUS-induced TME modifications. Further testing is required to characterize the levels in more samples for UTTs, MTTs, CLT-Ms, HTTs, and CLT-Hs. Future experiments with the CBA enhanced sensitivity flex sets will include IFN-γ in addition to the six cytokines tested previously.

Scope of Work

Combining immunology, biology, imaging, and engineering, this project would not have been possible without the multidisciplinary team of collaborative experts. The animal treatments and corresponding collection of data is enumerated in Table 3. The treatment types include: none (untreated), mFUS-high, mFUS-low, and hFUS. Tissue samples which will be processed by flow cytometry include 3 spleens from untreated mice, 2 mFUS-low treated tumors and their 2 corresponding spleens. Refrigerated maintenance was unsuccessful for tissues from 9 untreated mice and 11 hFUS-treated mice. Samples required for histology, IHC, and cytokine analysis are available for all 36 mice, and processing of these samples is currently underway.

Table 3. Summary of mice used for FUS treatments, IVIS imaging, and flow cytometry.

Treatment	IVIS	Flow Cytometry		Total (Mice)
		Treated tumor (UTT, MTT, & HTT)	Spleen	
None	4	6	6	15
mFUS-high	5	6	6	6
mFUS-low	0	2	2	4
hFUS	6	0	0	11
Total (Data)	15	14	14	**36**

Outcomes and Impact

We have developed the PyNGL model, the first-ever tool for monitoring whole tissue NF-κB activation in a spontaneous model of breast cancer. This model is particularly useful in our study, in which two forms of FUS, hFUS and mFUS, were administered to tumors as a source of inflammatory stimulus. The spontaneous nature of the tumors, and their subsequent metastatic progression, more closely model certain aspects of human disease than many orthotopic and cell line tumor models. Furthermore, the

PyNGL model maintains an intact immune system, allowing interactions between innate and adaptive immune cells, a crucial factor for assessing therapeutic response.

Using BLI as a method for non-destructive, *in vivo* imaging, snapshots of NF-κB activity at multiple time points before and after treatment enables assessment of temporal response. As with other detection techniques, a tradeoff between sensitivity and specificity exists; the ubiquitous presence of the NF-κB pathway in all cells lends itself to high sensitivity for a variety of therapeutic response mechanisms, with low specificity for distinguishing the type of response. However, the presence of the reporter transgene in all cells of the PyNGL model creates a window to monitor both local and systemic changes, which would not be possible with the use of a wild-type mouse developing tumors with a tumor cell-specific reporter transgene. As a consequence, background NF-κB activity, particularly high in the tumors, creates noisy data and images. Development of the described data acquisition and normalization techniques provides a method for improved sensitivity detection of changes from baseline, some of which may not be discernable with visual inspection of the images. The PyNGL model was developed as a tool to more efficiently inform therapeutic studies for use in tandem with advanced response characterization techniques.

Flow cytometry analysis of tumors and spleens reveal mFUS-induced changes in immune profile. The distinction of responders and non-responders may indicate that the response mechanism or timeline is varied between animals, and pre-treatment immunogenicity may play a role in treatment response. While the 48-hour time point may be optimal for NF-κB activation, the cellular immune response may lag temporally. Collection of tissues at additional time points, survival studies, and combination therapy with FUS and immunomodulatory agents are necessary to definitively characterize the impact of mFUS therapy. Additionally, assessment of cytokines within the tumors, as well as further classification of CD4+ T cells into helper and regulatory categories, will provide more insight into the tumor immunity response mechanisms.

REFERENCES

1. Sledge, G. W. *et al.* Past , Present , and Future Challenges in Breast Cancer Treatment. *J. Clin. Oncol.* **32,** 1979–1986 (2014).

2. Santa-Maria, C. A. & Gradishar, W. J. Changing Treatment Paradigms in Metastatic Breast Cancer: Lessons Learned. *JAMA Oncol.* **1,** 528–534 (2015).

3. Tinoco, G., Warsch, S., Glück, S., Avancha, K. & Montero, A. J. Treating Breast Cancer in the 21st Century : Emerging Biological Therapies. *J. Cancer* **4,** 117–132 (2013).

4. Gajewski, T. F. *et al.* Cancer immunotherapy strategies based on overcoming barriers within the tumor microenvironment. *Curr. Opin. Immunol.* **25,** 268–276 (2013).

5. McCarthy, E. F. The toxins of William B. Coley and the treatment of bone and soft-tissue sarcomas. *Iowa Orthop. J.* **26,** 154–158 (2006).

6. Jessy, T. Immunity over inability: The spontaneous regression of cancer. *J. Nat. Sci. Biol. Med.* **2,** 43 (2011).

7. Li, Z., Chen, L. & Rubinstein, M. P. Cancer immunotherapy: are we there yet? *Exp. Hematol. Oncol.* **2,** 33 (2013).

8. Scott, A. M., Wolchok, J. D. & Old, L. J. Antibody therapy of cancer. *Nat. Rev. Cancer* **12,** 278–287 (2012).

9. Sliwkowski, M. X. & Mellman, I. Antibody therapeutics in cancer. *Science (80-.).* **341,** 1192–8 (2013).

10. Restifo, N. P., Dudley, M. E. & Rosenberg, S. a. Adoptive immunotherapy for cancer: harnessing the T cell response. *Nat. Rev. Immunol.* **12,** 269–281 (2012).

11. Harris, T. J. & Drake, C. G. Primer on tumor immunology and cancer immunotherapy. *J. Immunother. cancer* **1,** 12 (2013).

12. Mellman, I., Coukos, G. & Dranoff, G. Cancer immunotherapy comes of age. *Nature* **480,** 480–489 (2011).

13. Friedman, E. J. Immune modulation by ionizing radiation and its implications for cancer immunotherapy. *Curr. Pharm. Des.* **8,** 1765–1780 (2002).

14. Kaminski, J. M. *et al.* The controversial abscopal effect. *Cancer Treat. Rev.* **31,** 159–172 (2005).

15. Demaria, S. *et al.* Ionizing radiation inhibition of distant untreated tumors (abscopal effect) is immune mediated. *Int. J. Radiat. Oncol. Biol. Phys.* **58,** 862–870 (2004).

16. Formenti, S. C. & Demaria, S. Systemic effects of local radiotherapy. *Lancet Oncol.* **10,** 718–726 (2009).

17. Paliwal, S. & Mitragotri, S. Therapeutic opportunities in biological responses of ultrasound. *Ultrasonics* **48,** 271–278 (2008).

18. *The breast cancer landscape*. *Department of Defense Breast Cancer Research Program* (2014). doi:10.1038/486328a

19. Polyak, K. Heterogeneity in breast cancer. *J. Clin. Invest.* **121,** 3786–3788 (2011).

20. Welch, H. G., Gorski, D. H. & Albertsen, P. C. Trends in Metastatic Breast and Prostate Cancer - Lessons in Cancer Dynamics. *N. Engl. J. Med.* **373,** 1685–1687 (2015).

21. *Diseases of the Breast*. (J.B. Lippincott, Williams, & Wilkins, 2000).

22. Pal, S. K. *et al.* Lack of survival benefit in metastatic breast cancer with newer chemotherapy agents: The City of Hope cancer experience. in *American Society of Clinical Oncology Annual Meeting* (2008).

23. Sompayrac, L. *How the Immune System Works*. (2012).

24. Delves, P. & Martin, S. *Roitt's Essential Immunology*. (Wiley-Blackwell, 2011).

25. Janeway, C., Travers, P., Walport, M. & Shlomchik, M. *Immunobiology: The Immune System in Health and Disease*. (Garland Science: Taylor & Francis Group, 2004).

26. Houghton, A. N. & Guevara-Patiño, J. a. Immune recognition of self in immunity against cancer. *J. Clin. Invest.* **114,** 468–471 (2004).

27. Zou, W. Immunosuppressive networks in the tumour environment and their therapeutic relevance. *Nat. Rev. Cancer* **5,** 263–274 (2005).

28. Dunn, G. P., Bruce, A. T., Ikeda, H., Old, L. J. & Schreiber, R. D. Cancer immunoediting: from immunosurveillance to tumor escape. *Nat. Immunol.* **3,** 991–998 (2002).

29. Schreiber, R. D., Old, L. J. & Smyth, M. J. Cancer immunoediting: integrating immunity's roles in cancer suppression and promotion. *Science* **331,** 1565–1570 (2011).

30. Vesely, M. D., Kershaw, M. H., Schreiber, R. D. & Smyth, M. J. Natural innate and adaptive immunity to cancer. *Annu. Rev. Immunol.* **29,** 235–271 (2011).

31. Hanahan, D. & Coussens, L. M. Accessories to the Crime: Functions of Cells Recruited to the Tumor Microenvironment. *Cancer Cell* **21,** 309–322 (2012).

32. Neĭman, I. M. Inflammation and cancer. *Patol. Fiziol. Eksp. Ter.* **420,** 3–5 (2002).

33. Ortega, R. a *et al.* Biocompatible mannosylated endosomal-escape nanoparticles enhance selective delivery of short nucleotide sequences to tumor associated macrophages. *Nanoscale* **7,** 500–510 (2015).

34. DeNardo, D. G. & Coussens, L. M. Inflammation and breast cancer. Balancing immune response: crosstalk between adaptive and innate immune cells during breast cancer progression. *Breast Cancer Res.* **9,** 212 (2007).

35. Burnet, M. Cancer - A biological approach: I. The processes of control. *Br Med J* **1,** 779–786 (1957).

36. Creative Commons Legal Code: Attribution 4.0 International. *Creative Commons Corporation* 1–5 (2016). at <https://creativecommons.org/licenses/by/4.0/legalcode>

37. Reslan, L., Dalle, S. & Dumontet, C. Understanding and circumventing resistance to anticancer monoclonal antibodies. *MAbs* **1,** 222–229 (2009).

38. ter Haar, G. Therapeutic applications of ultrasound. *Prog. Biophys. Mol. Biol.* **93,** 111–129 (2007).

39. Wood, R. W. & Loomis, A. L. The physical and biological effects of high frequency sound waves of great intensity. *Philos. Mag. J. Sci.* **4,** 151–153 (1927).

40. Yu, T., Wang, Z. & Mason, T. J. A review of research into the uses of low level ultrasound in cancer therapy. *Ultrason. Sonochem.* **11,** 95–103 (2004).

41. Mason, T. J. Therapeutic ultrasound an overview. *Ultrason. Sonochem.* **18,** 847–852 (2011).

42. Mitragotri, S., Blankschtein, D. & Langer, R. Ultrasound-mediated transdermal protein delivery. *Science* **269,** 850–853 (1995).

43. Everbach, E. & Francis, C. Cavitation mechanisms in ultrasound-accelerated thrombolysis at 1 MHz. *Ultrasound Med. Biol.* **26,** 1153–1160 (2000).

44. Barnett, S. B. *et al.* Current status of research on biophysical effects of ultrasound. *Ultrasound Med. Biol.* **20,** 205–218 (1994).

45. Barnett, S. B., Rott, H. D., Ter Haar, G. R., Ziskin, M. C. & Maeda, K. The sensitivity of biological tissue to ultrasound. *Ultrasound Med. Biol.* **23,** 805–812 (1997).

46. ter Haar, G. Therapeutic ultrasound. *Eur. J. Ultrasound* **9,** 3–9 (1999).

47. Van Rhoon, G. C. *et al.* CEM43°C thermal dose thresholds: A potential guide for magnetic resonance radiofrequency exposure levels? *Eur. Radiol.* **23,** 2215–2227 (2013).

48. Dieing, A. *et al.* The effect of induced hyperthermia on the immune system. *Prog. Brain Res.* **162,** 137–152 (2007).

49. Sapareto, S. A. (Wayne S. U. M. S. & Dewey, W. C. (University of C. C. 200). Thermal dose determination in cancer therapy. *J. Radiat. Oncol.* **10,** 787–800 (1984).

50. McDannold, N. *et al.* Uterine leiomyomas: MR imaging-based thermometry and thermal dosimetry during focused ultrasound thermal ablation. *Radiology* **240,** 263–272 (2006).

51. Rieke, V. & Pauly, K. B. MR thermometry. *J. Magn. Reson. Imaging* **27,** 376–390 (2008).

52. Al-bataineh, O., Jenne, J. & Huber, P. Clinical and future applications of high intensity focused ultrasound in cancer. *Cancer Treat. Rev.* **38,** 346–353 (2012).

53. Hazle, J. D., Jason Stafford, R. & Price, R. E. Magnetic resonance imaging-guided focused ultrasound thermal therapy in experimental animal models: Correlation of ablation volumes with pathology in rabbit muscle and VX2 tumors. *J. Magn. Reson. Imaging* **15,** 185–194 (2002).

54. Unga, J. & Hashida, M. Ultrasound induced cancer immunotherapy. *Adv. Drug Deliv. Rev.* **72,** 144–153 (2014).

55. Baker, K. G., Robertson, V. J. & Duck, F. a. A review of therapeutic ultrasound: biophysical effects. *Phys. Ther.* **81,** 1351–1358 (2001).

56. Mitragotri, S. Healing sound: the use of ultrasound in drug delivery and other therapeutic applications. *Nat. Rev. Drug Discov.* **4,** 255–260 (2005).

57. Dalecki, D. Mechanical bioeffects of ultrasound. *Annu. Rev. Biomed. Eng.* **6,** 229–248 (2004).

58. Tung, Y. S. *et al.* Contrast-agent-enhanced ultrasound thermal ablation. *Ultrasound Med. Biol.* **32,** 1103–1110 (2006).

59. Kuroda, K., Chung, A. H., Hynynen, K. & Jolesz, F. A. Calibration of Water Proton Chemical Shift with Temperature for Noninvasive Temperature Imaging During Focused Ultrasound Surgery. *JMRI* **8,** 175–181 (1998).

60. Hu, Z. *et al.* Release of endogenous danger signals from HIFU-treated tumor cells and their stimulatory effects on APCs. *Biochem Biophys Res Commun* **335,** 124–131 (2005).

61. Hu, Z. *et al.* Investigation of HIFU-induced anti-tumor immunity in a murine tumor model. *J. Transl. Med.* **5,** 34 (2007).

62. Liu, F. *et al.* Boosting high-intensity focused ultrasound-induced anti-tumor immunity using a sparse-scan strategy that can more effectively promote dendritic cell maturation. *J. Transl. Med.* **8,** (2010).

63. Zhang, H. G., Mehta, K., Cohen, P. & Guha, C. Hyperthermia on immune regulation: A temperature's story. *Cancer Lett.* **271,** 191–204 (2008).

64. Kheirolomoom, A. *et al.* CpG expedites regression of local and systemic tumors when combined with activatable nanodelivery. *J. Control. Release* **220 A,** 253–264 (2015).

65. Yang, B. R. *et al.* Effects of High-Intensity Focused Ultrasound in the Treatment Experimental Neuroblastoma. *J. Pediatr. Surg.* **27,** 246–251 (1992).

66. Zhang, Y., Deng, J., Feng, J. & Wu, F. Enhancement of antitumor vaccine in ablated hepatocellular carcinoma by high-intensity focused ultrasound. *World J Gastroenterol* **16,** 3584–3591 (2010).

67. Karin, M. NF- B as a Critical Link Between Inflammation and Cancer. *Cold Spring Harb. Perspect. Biol.* **1,** a000141–a000141 (2009).

68. Carlsen, H., Moskaug, J., Fromm, S. H. & Blomhoff, R. In Vivo Imaging of NF- κ B Activity. *J. Immunol.* **168,** 1441–1446 (2002).

69. Gerondakis, S. & Siebenlist, U. Roles of the NF-kB Pathway in Lymphocyte Development and Function. *Cold Spring Harb. Perspect. Biol.* **2,** 1–29 (2010).

70. Dolcet, X., Llobet, D., Pallares, J. & Matias-Guiu, X. NF-kB in development and progression of human cancer. *Virchows Arch* **446,** 475–482 (2005).

71. Rosenberg, S. a, Yang, J. C. & Restifo, N. P. Cancer immunotherapy: moving beyond current vaccines. *Nat. Med.* **10,** 909–915 (2004).

72. Gao, J., Bernatchez, C., Sharma, P., Radvanyi, L. G. & Hwu, P. Advances in the development of cancer immunotherapies. *Trends Immunol.* **34,** 90–98 (2013).

73. Ogino, S., Galon, J., Fuchs, C. S. & Dranoff, G. Cancer immunology - analysis of host and tumor factors for personalized medicine. *Nat Rev Clin Oncol* **8,** 711–719 (2012).

74. Whiteside, T. L. The tumor microenvironment and its role in promoting tumor growth. *Oncogene* **27,** 5904–5912 (2008).

75. Mbeunkui, F. & Johann, D. J. Cancer and the tumor microenvironment: a review of an essential relationship. *Cancer Chemother Pharmacol* **63,** 571–582 (2009).

76. Yu, H., Kortylewski, M. & Pardoll, D. Crosstalk between cancer and immune cells: role of STAT3 in the tumour microenvironment. *Nat. Rev. Immunol.* **7,** 41–51 (2007).

77. Palucka, K. & Banchereau, J. Dendritic-Cell-Based Therapeutic Cancer Vaccines. *Immunity* **39,** 38–48 (2013).

78. Van den Boorn, J. G. & Hartmann, G. Turning Tumors into Vaccines: Co-opting the Innate Immune System. *Immunity* **39,** 27–37 (2013).

79. Pardoll, D. M. The blockade of immune checkpoints in cancer immunotherapy. *Nat. Rev. Cancer* **12,** 252–264 (2012).

80. Eggermont, A. M. M., Kroemer, G. & Zitvogel, L. Immunotherapy and the concept of a clinical cure. *Eur. J. Cancer* **49,** 2965–2967 (2013).

81. Gao, Q. *et al.* Overexpression of PD-L1 significantly associates with tumor aggressiveness and postoperative recurrence in human hepatocellular carcinoma. *Clin. Cancer Res.* **15,** 971–979 (2009).

82. Rosenblatt, J. & Glotzbecker, B. PD-1 blockade by CT-011, anti PD-1 antibody, enhances ex-vivo T cell responses to autologous dendritic/myeloma fusion vaccine. *J. …* **34,** 409–418 (2011).

83. Ludewig, B. *et al.* In vivo antigen loading and activation of dendritic cells via a liposomal peptide vaccine mediates protective antiviral and anti-tumour immunity. *Vaccine* **19,** 23–32 (2000).

84. Wang, Z., Monte, D., Rewers-felkins, K. & Quinlin, I. Dendritic cells enhance the activity of human MUC1-stimulated mononuclear cells against breast cancer. 1–7 (2013).

85. Shortman, K. & Heath, W. R. The CD8 + dendritic cell subset. *Immunol. Rev.* **234,** 18–31 (2010).

86. Mogrão, J., da Costa, C. A., Gaspar, R. & Florindo, H. F. Modulation of Dendritic Cells by Nanotechnology-Based Immunotherapeutic Strategies. *J. Biomed. Nanotechnol.* **12,** 405–434 (2016).

87. Luo, Y. *et al.* Targeting tumor-associated macrophages as a novel strategy against breast cancer. *J. Clin. Invest.* **116,** 2132–2141 (2006).

88. Kabingu, E., Vaughan, L., Owczarczak, B., Ramsey, K. D. & Gollnick, S. O. CD8+ T cell-mediated control of distant tumours following local photodynamic therapy is independent of CD4+ T cells and dependent on natural killer cells. *Br. J. Cancer* **96,** 1839–1848 (2007).

89. Disis, M. L. Immune regulation of cancer. *J. Clin. Oncol.* **28,** 4531–4538 (2010).

90. Shah, W. *et al.* A reversed CD4/CD8 ratio of tumor-infiltrating lymphocytes and a high percentage of CD4(+)FOXP3(+) regulatory T cells are significantly associated with clinical outcome in squamous cell carcinoma of the cervix. *Cell. Mol. Immunol.* **8,** 59–66 (2011).

91. Mahmoud, S. M. a *et al.* Tumor-infiltrating CD8 + lymphocytes predict clinical outcome in breast cancer. *J. Clin. Oncol.* **29,** 1949–1955 (2011).

92. Lai, Y.-P., Jeng, C.-J. & Chen, S.-C. The roles of CD4+ T Cells in tumor immunity. *ISRN Immunol.* **2011,** doi:10.5402/2011/497397 (2011).

93. Kennedy, R. & Celis, E. Multiple roles for CD4+ T cells in anti-tumor immune responses. *Immunol Rev* **222,** 129–144 (2008).

94. Motz, G. & Coukos, G. Deciphering and Reversing Tumor Immune Suppression. *Immunity* **39,** 61–73 (2013).

95. Kim, H.-J. & Cantor, H. CD4 T-cell Subsets and Tumor Immunity: The Helpful and the Not-so-Helpful. *Cancer Immunol. Res.* **2,** 91–98 (2014).

96. Dobrzanski, M. J. Expanding roles for CD4 T cells and their subpopulations in tumor immunity and therapy. *Front. Oncol.* **3,** 63 (2013).

97. Lu, P. *et al.* Increased infiltration of activated tumor-infiltrating lymphocytes after high intensity focused ultrasound ablation of human breast cancer. *Surgery* **145,** 286–293 (2009).

98. Angell, H. & Galon, J. From the immune contexture to the Immunoscore: The role of prognostic and predictive immune markers in cancer. *Curr. Opin. Immunol.* **25,** 261–267 (2013).

99. Hanahan, D. & Weinberg, R. a. Hallmarks of cancer: The next generation. *Cell* **144,** 646–674 (2011).

100. Salgado, R. *et al.* The evaluation of tumor-infiltrating lymphocytes (TILS) in breast cancer: Recommendations by an International TILS Working Group 2014. *Ann. Oncol.* **26,** 259–271 (2015).

101. Galon, J. *et al.* Cancer classification using the Immunoscore: a worldwide task force. *J. Transl. Med.* **10,** 205 (2012).

102. Galon, J., Angell, H., Bedognetti, D. & Marincola, F. The Continuum of Cancer Immunosurveillance: Prognostic, Predictive, and Mechanistic Signatures. *Immunity* **39,** 11–26 (2013).

103. Lee, S. & Margolin, K. Cytokines in cancer immunotherapy. *Cancers (Basel).* **3,** 3856–93 (2011).

104. Dranoff, G. Cytokines in cancer pathogenesis and cancer therapy. *Nat. Rev. Cancer* **4,** 11–22 (2004).

105. Fisher, D. T., Appenheimer, M. M. & Evans, S. S. The two faces of IL-6 in the tumor microenvironment. *Semin. Immunol.* **26,** 38–47 (2014).

106. Wilke, C. M. *et al.* Th17 cells in cancer: Help or hindrance? *Carcinogenesis* **32,** 643–649 (2011).

107. Creative Commons Legal Code: Attribution-NonCommerial-ShareAlike 3.0 Unported. *Creative Commons Corporation* 9–12 (2011). at <https://creativecommons.org/licenses/by-nc-sa/3.0/legalcode>

108. Klerk, C. P. W. *et al.* Validity of bioluminescence measurements for noninvasive in vivo imaging of tumor load in small animals. *Biotechniques* **43,** 7–13 (2007).

109. Zinn, K. R. *et al.* Noninvasive Bioluminescence Imaging in Small Animals. *ILAR J.* **49,** 103–115 (2008).

110. Neill, K. O., Lyons, S. K., Gallagher, W. M., Curran, K. M. & Byrne, A. T. Bioluminescent imaging : a critical tool in pre-clinical oncology research. *J. Pathol.* **220,** 317–327 (2010).

111. Choy, G. *et al.* Comparison of noninvasive fluorescent and bioluminescent small animal optical imaging. *Biotechniques* **35,** 1022–1030 (2003).

112. Everhart, M. B. *et al.* Duration and Intensity of NF-kB Activity Determine the Severity of Endotoxin-Induced Acute Lung Injury. *J. Immunol.* **176,** 4995–5005 (2006).

113. Roth, D. J., Jansen, E. D., Powers, A. C. & Wang, T. G. A Novel Method of Monitoring Response to Islet Transplantation: Bioluminescent Imaging of an NF-kB Transgenic Mouse Model. *Transplantation* **81,** 1185–1190 (2006).

114. Park, D. *et al.* Optical Imaging of Treatment-Related Tumor Cell Death Using a Heat Shock Protein-90 Alkylator. *Mol. phamaceutics* **10,** 3882–3891 (2013).

115. Au, J. T., Gonzalez, L., Chen, C., Serganova, I. & Fong, Y. Bioluminescence Imaging Serves as a Dynamic Marker for Guiding and Assessing Thermal Treatment of Cancer in a Preclinical Model. *Ann. Surg. Oncol.* **19,** 3116–3122 (2012).

116. May, M. J. & Ghosh, S. Signal transduction through NF-kB. *Immunol. Today* **19,** 80–88 (1998).

117. Schmitz, M. L. Function and activation of the transcription factor NF-KB in the response to toxins and pathogens. *Toxicol. Lett.* **82/83,** 407–411 (1995).

118. Barnes, P. J. Nuclear Factor-kB. *Int. J. Biochem. Cell Biol.* **29,** 867–870 (1997).

119. Baldwin, A. S. Control of oncogenesis and cancer therapy resistance by the transcription factor NF-κB. *J. Clin. Invest.* **107,** 241–246 (2001).

120. Connelly, L. *et al.* A transgenic model reveals important roles for the NF-kB alternative pathway (p100/p52) in mammary development and links to tumorigenesis. *J. Biol. Chem.* **282,** 10028–10035 (2007).

121. Jing, H. *et al.* Opposing roles of NF-kB in anti-cancer treatment outcome unveiled by cross-species investigations. *Cold Spring Harb. Lab. Press* **25,** 2137–2146 (2011).

122. Hoesel, B. & Schmid, J. a. The complexity of NF-κB signaling in inflammation and cancer. *Mol. Cancer* **12,** 86 (2013).

123. Karin, M. NF-kB as a Critical Link Between Inflammation and Cancer. *Cold Spring Harb. Perspect. Biol.* **1,** a000141 (2009).

124. Gerondakis, S., Fulford, T. S., Messina, N. L. & Grumont, R. J. NF-κB control of T cell development. *Nat. Immunol.* **15,** 15–25 (2014).

125. Li, F. & Sethi, G. Targeting transcription factor NF-κB to overcome chemoresistance and radioresistance in cancer therapy. *BBA - Rev. Cancer* **1805,** 167–180 (2010).

126. Lin, E. Y. *et al.* Progression to malignancy in the polyoma middle T oncoprotein mouse breast cancer model provides a reliable model for human diseases. *Am. J. Pathol.* **163,** 2113–2126 (2003).

127. Burgos, J. S. *et al.* Time Course of Bioluminescent Signal in Orthotopic and Heterotopic Brain Tumors in Nude Mice. *Biotechniques* **34,** 1184–1188 (2003).

128. Inoue, Y., Kiryu, S., Watanabe, M., Tojo, A. & Ohtomo, K. Timing of Imaging after D-Luciferin Injection Affects the Longitudinal Assessment of Tumor Growth Using In Vivo Bioluminescence Imaging. *Int. J. Biomed. Imaging* **2010,** doi:10.1155/2010/471408 (2010).

129. Poorman, M. E. *et al.* Open-source, small-animal magnetic resonance-guided focused ultrasound

system. *J. Ther. Ultrasound* **4,** DOI 10.1186/s40349-016-0066-7 (2016).

130. Maxwell, A. D. *et al.* Cavitation clouds created by shock scattering from bubbles during histotripsy. *J. Acoust. Soc. Am.* **130,** 1888–98 (2011).

131. Jahan-tigh, R. R., Ryan, C., Obermoser, G. & Schwarzenberger, K. Flow Cytometry. *J. Invest. Dermatol.* **132,** e1-6 (2012).

132. Holmes, D. *et al.* Leukocyte analysis and differentiation using high speed microfluidic single cell impedance cytometry. *Lab Chip* **9,** 2881–2889 (2009).

133. Groen, B. *et al.* Immunological Adaptations to Pregnancy in Women with Type 1 Diabetes. *Sci. Rep.* **5,** doi: 10.1038/srep13618 (2015).

134. BD Biosciences. BD Cytometric Bead Array (CBA) Mouse Enhanced Sensitivity Master Buffer Kit: Instruction Manual. (2011). at <http://www.bdbiosciences.com/external_files/Doc_Recon_2.0/pm/others/23-13336.pdf>

135. Zhao, L., Liu, L., Guo, B. & Zhu, B. Regulation of adaptive immune responses by guiding cell movements in the spleen. *Front. Microbiol.* **6,** doi: 10.3389/fmicb.2015.00645 (2015).

136. Bronte, V. & Pittet, M. J. The spleen in local and systemic regulation of immunity. *Immunity2* **39,** 806–818 (2013).

137. Elmore, S. A. *et al.* Recommendations from the INHAND Apoptosis / Necrosis Working Group. *Toxicol. Pathol.* **44,** 173–88 (2016).

138. Rock, K. L. & Kono, H. The inflammatory response to cell death. *Annu Rev Pathol.* **3,** 99–126 (2008).

139. Drescher, K. M. & Lynch, H. T. Tumor infiltrating lymphocytes (TILs): Lessons learned in 30 years of study. *Clin. Appl. Immunol. Rev.* **5,** 149–166 (2005).

140. Zhou, P., Fu, M., Bai, J., Wang, Z. & Wu, F. Immune response after high-intensity focused ultrasound ablation for H22 tumor. *J. Clin. Oncol. ASCO 2007 Annu. Meet. Proc. (Post-Meeting Ed.* **25,** 21169 (2007).